

## REPORT DOCUMENTATION PAGE

*Form Approved  
OMB No. 0704-0188*

The public reporting burden for this collection of information is estimated to average 1 hour per response, including the time for reviewing instructions, searching existing data sources, gathering and maintaining the data needed, and completing and reviewing the collection of information. Send comments regarding this burden estimate or any other aspect of this collection of information, including suggestions for reducing the burden, to Department of Defense, Washington Headquarters Services, Directorate for Information Operations and Reports (0704-0188), 1215 Jefferson Davis Highway, Suite 1204, Arlington, VA 22202-4302. Respondents should be aware that notwithstanding any other provision of law, no person shall be subject to any penalty for failing to comply with a collection of information if it does not display a currently valid OMB control number.

**PLEASE DO NOT RETURN YOUR FORM TO THE ABOVE ADDRESS.**

|   |                  |                            |                                      |  |   |
|---|------------------|----------------------------|--------------------------------------|--|---|
| 1. REPORT DATE (DD-MM-YYYY)   | 2. REPORT TYPE   |                            | 3. DATES COVERED (From - To)         |  |   |
| 15-03-2011  | Final Report     |                            | 25-03-2008 -- 30-06-2011             |  |   |
| 4. TITLE AND SUBTITLE   |                  |                            | 5a. CONTRACT NUMBER                  |  |   |
| Synthetic Aperture Sonar Imaging of Simple Finite Targets   |                  |                            | 5b. GRANT NUMBER<br>N00014-07-G-0557 |  |   |
|   |                  |                            | 5c. PROGRAM ELEMENT NUMBER           |  |   |
| 6. AUTHOR(S)  |                  |                            | 5d. PROJECT NUMBER                   |  |   |
| Steven G. Kargl, Kevin L. Williams, Eric. I. Thorsos  |                  |                            | 5e. TASK NUMBER                      |  |   |
|   |                  |                            | 5f. WORK UNIT NUMBER                 |  |   |
| 7. PERFORMING ORGANIZATION NAME(S) AND ADDRESS(ES)  |                  |                            |                                      | 8. PERFORMING ORGANIZATION REPORT NUMBER           |   |
| Applied Physics Laboratory<br>University of Washington<br>1014 NE 40th St.<br>Seattle, WA 98105   |                  |                            |                                      |  |   |
| 9. SPONSORING/MONITORING AGENCY NAME(S) AND ADDRESS(ES)   |                  |                            |                                      | 10. SPONSOR/MONITOR'S ACRONYM(S)<br>ONR            |   |
| Office of Naval Research<br>One Liberty Center<br>875 North Randolph Street<br>Arlington, VA 22203  |                  |                            |                                      | 11. SPONSOR/MONITOR'S REPORT NUMBER(S)             |   |
| 12. DISTRIBUTION/AVAILABILITY STATEMENT<br>Distribution Statement A: Approved for public release, distribution unlimited.   |                  |                            |                                      |  |   |
| 13. SUPPLEMENTARY NOTES   |                  |                            |                                      |  |   |
| 14. ABSTRACT<br>During the Sediment Acoustics Experiment 2004 (SAX04), a synthetic aperture sonar (SAS) was used to detect simple targets that were either proud or buried below a water-sediment interface, where the nominal grazing angle of incidence from the SAS to the point above a buried target was well below the critical grazing angle. SAS images from other measurements below the critical angle have also produced target detections of buried spheres and finite cylinders. Models and numerical simulations are developed to investigate these proud and buried target detections. For buried targets, the simulations include estimates of reverberation from the rough seafloor, the subcritical penetration through the seafloor, scattering from a target, and propagation back to the SAS. For proud targets, the simulations include the scattering from the target where interaction with the seafloor is included through simple ray models. The simulations used environmental and material parameters measured during SAX04. The environmental measurements include profiles of small-scale surface roughness and superimposed ripple structure. The SAS simulations and model/measurement comparisons over a frequency range of 10–50 kHz further support scattering from sediment ripple structure as the dominant mechanism for subcritical penetration in this range. $11n(1-h)$ . The approach toward equilibrium, as measured <del>the coantillation index is exponential: <math>12 \ln(1-h) + 1 + O(h^{-2})</math>. This provides a</del> |                  |                            |                                      |  |   |
| 15. SUBJECT TERMS<br>Synthetic aperture sonar, acoustic scattering, ripple, signal-to-noise ration (SNR)  |                  |                            |                                      |  |   |
| 16. SECURITY CLASSIFICATION OF:   |                  | 17. LIMITATION OF ABSTRACT | 18. NUMBER OF PAGES                  | 19a. NAME OF RESPONSIBLE PERSON<br>Steven G. Kargl |   |
| a. REPORT<br>U  | b. ABSTRACT<br>U | c. THIS PAGE<br>U          | U                                    | 41   | 19b. TELEPHONE NUMBER (Include area code)<br>(206) 685-4677 |

Reset

Standard Form 298 (Rev. 8/98)  
Prescribed by ANSI Std. Z39-18

# Synthetic Aperture Sonar Imaging of Simple Finite Targets

Steven G. Kargl, Kevin L. Williams, and Eric I. Thorsos

## Abstract

During the Sediment Acoustics Experiment 2004 (SAX04), a synthetic aperture sonar (SAS) was used to detect simple targets that were either proud or buried below a water-sediment interface, where the nominal grazing angle of incidence from the SAS to the point above a buried target was well below the critical grazing angle. SAS images from other measurements below the critical angle have also produced target detections of buried spheres and finite cylinders. Models and numerical simulations are developed to investigate these proud and buried target detections. For buried targets, the simulations include estimates of reverberation from the rough seafloor, the subcritical penetration through the seafloor, scattering from a target, and propagation back to the SAS. For proud targets, the simulations include the scattering from the target where interaction with the seafloor is included through simple ray models. The simulations used environmental and material parameters measured during SAX04. The environmental measurements include profiles of small-scale surface roughness and superimposed ripple structure. The SAS simulations and model/measurement comparisons over a frequency range of 10–50 kHz further support scattering from sediment ripple structure as the dominant mechanism for subcritical penetration in this range.

## Index Terms

Synthetic aperture sonar, acoustic scattering, ripple, signal-to-noise ratio (SNR)

## I. INTRODUCTION

Synthetic aperture sonar (SAS) systems are becoming a common tool in underwater acoustics, a particular example being systems designed to detect mines in shallow water [1], [2]. In such environments the water-sediment interface invariably plays a role, affecting both the signal

from the target being detected and contributing to the noise that masks this signal. Thus, understanding and modeling the acoustic processes at the water-sediment interface and simulating SAS operation in the presence of this interface are important.

The primary goals of this work are to summarize the modeling techniques used to quantitatively understand SAS imaging of simple proud and buried targets and compare modeling results to field data. The model development was motivated by the specific problem of shallow grazing angle detection of buried targets at frequencies below 50 kHz. However, the more general objective of incorporating the environment into a “single realization” modeling capability needed to generate SAS images was equally important. Thus several problems of increasing complexity are examined here starting with SAS imaging of freefield targets and ending with the buried target problem.

The field data used for comparisons with modeling results were obtained during the Sediment Acoustics Experiment in 2004 (SAX04) [3]. SAX04 was conducted in the Gulf of Mexico about 1 km offshore near Fort Walton Beach, Florida in 17–18 m of water. The SAS measurements were made using a 28 m rail system [4] deployed on the sea floor.

Finite element modeling (FEM) can also be applied to model with high fidelity scattering from proud and buried targets (e.g., see [5]). However, the FEM approach is computationally intensive, and therefore its application to SAS imaging that involves Fourier synthesis to model each transmission would be especially challenging. The approach being described here involves a more approximate treatment of target scattering, but has the advantage of much better computational efficiency than for the FEM method.

## II. MODEL DESCRIPTIONS

Several independent models have been combined to produce a single model, which can be used to generate a set of signals for SAS processing. This section describes these models and some of the underlying assumptions and approximations.

The origin of the coordinate geometry for the reverberation and penetration models lies in the mean water-sediment interface. The  $z$ -axis is oriented perpendicular to this interface such that its unit vector,  $\hat{z}$ , points towards the air-water interface. The  $x$ -axis coincides with the range coordinate of the SAS. The  $y$ -axis is aligned with the direction of travel of the SAS, sometimes called the along-track direction or dimension. Throughout this article, the  $y$ -axis will be referred to as the cross range direction or simply as cross range. For a given signal, the locations of

the source, receiver, and target are given by  $\mathbf{r}_{src} = (x_{src}, y_{src}, z_{src})$ ,  $\mathbf{r}_{rcv} = (x_{rcv}, y_{rcv}, z_{rcv})$ , and  $\mathbf{r}_{tgt} = (x_{tgt}, y_{tgt}, z_{tgt})$ , respectively. For the surface integrals to be defined shortly, capital bold symbols denote horizontal vectors (i.e.,  $\mathbf{r} = \mathbf{R} + z\hat{\mathbf{z}}$ ).

For the SAX04 experiment and the simulations to be discussed below, interaction of the acoustic field with the air-water interface does not occur in the time interval of interest. Thus, the model assumes semi-infinite inviscid water above a semi-infinite fluid sediment. The sound speed and density in the water are  $c_1$  and  $\rho_1$ ; while the sound speed, density, and dimensionless loss parameter for the sediment are  $c_2$ ,  $\rho_2$ , and  $\delta_2$ , respectively [6].

### A. Reverberation

A time domain reverberation model has recently been developed, based on first-order perturbation theory, to describe sound scattering from a rough seafloor. A derivation of this model is given in Appendix I. Several approximations are employed in addition to first-order perturbation theory: the stationary phase approximation is used to evaluate the zero-order field needed for the first-order theory, the sound speed in the sediment is approximated as independent of frequency, the attenuation in the sediment is approximated as linearly increasing with frequency, and the frequency dependence of the source and receive beam patterns is neglected. The latter approximation is reasonably satisfied for our measurements because the horizontal aperture of the source, composed of four transducers in a compact horizontal array, is steadily reduced as the frequency is increased by reducing the number of active elements from four down to one in steps. For bistatic backscattering in the incident vertical plane [see the discussion near (I.40)], this model reduces to the following surface integral over the mean plane of the water-sediment interface:

$$\begin{aligned} p_{rev}(\mathbf{r}_{rcv}, t) &= \frac{1}{4\pi c_1^2} \\ &\times \int d^2 R \frac{A_{rev}(\mathbf{R}) h(\mathbf{R}) \ddot{p}_{src}(t - t_{rev})}{|\mathbf{r}_{rcv} - \mathbf{R}| |\mathbf{R} - \mathbf{r}_{src}|}. \end{aligned} \quad (1)$$

Here, and throughout this article, the assumed time convention is  $\exp(-\omega t)$  with  $t$  and  $\omega$  denoting time and angular frequency. In (1) the subscript *rev* denotes quantities related to reverberation, that is, sound scattering from the rough water-sediment interface. Environmental

and system parameters enter into the formulation through the complex coefficient

$$\begin{aligned} A_{rev}(\mathbf{R}) = & r_0 B_{src} B_{rcv} \{ [1 + \Gamma_{11}(\theta_i)][1 + \Gamma_{11}(\theta_s)] \\ & \times (1 - \kappa^2/\rho) + (\rho - 1)[1 - \Gamma_{11}(\theta_i)][1 - \Gamma_{11}(\theta_s)] \\ & \times \sin \theta_i \sin \theta_s + (1 - 1/\rho)[1 + \Gamma_{11}(\theta_i)][1 + \Gamma_{11}(\theta_s)] \\ & \times \cos \theta_i \cos \theta_s \}, \end{aligned} \quad (2)$$

where  $B_{src}$ ,  $B_{rcv}$ ,  $\theta_i$ ,  $\theta_s$ , and  $\Gamma_{11}(\theta)$  depend on  $\mathbf{R}$ . The source and receiver response functions evaluated at  $\mathbf{R}$  on the mean surface plane are  $B_{src}$  and  $B_{rcv}$ , respectively. (The beam patterns are the square of the response functions.) The incident and scattered grazing angles are determined by  $\sin \theta_i = z_{src}/|\mathbf{R} - \mathbf{r}_{src}|$  and  $\sin \theta_s = z_{rcv}/|\mathbf{r}_{rcv} - \mathbf{R}|$ , respectively. The plane-wave reflection coefficient at grazing angle  $\theta$  is

$$\Gamma_{11}(\theta) = \frac{\rho \sin \theta - (\kappa^2 - \cos^2 \theta)^{1/2}}{\rho \sin \theta + (\kappa^2 - \cos^2 \theta)^{1/2}}. \quad (3)$$

In (3)  $\rho = \rho_2/\rho_1$  and  $\kappa = k_2/k_1 = (1 + i\delta_2)/\nu$ , where  $\nu = c_2/c_1$  is the real index of refraction. (The subscripts on  $\Gamma_{11}(\theta)$  denote that both the ingoing and outgoing fields are in the water (medium 1), in contrast to the transmission coefficient introduced in Sec. II-B.) Finally,  $r_0 = 1$  m has been introduced into (2) to preserve dimensional consistency in (1). In (1),  $h(\mathbf{R})$  is the local height of the water-sediment interface relative to the mean plane, and  $p_{src}(t)$  is the pressure field at 1 m from the source on the transmit beam axis. The double dot notation indicates the second derivative with respect to time. Finally, the round-trip time delay to propagate from the source to the point  $\mathbf{R}$  on the mean plane and then back to the receiver is  $t_{rev} = (|\mathbf{r}_{rcv} - \mathbf{R}| + |\mathbf{R} - \mathbf{r}_{src}|)/c_1$ .

### B. Penetration

Thorsos *et al.* [6] proposed rough surface scattering as a mechanism to explain the significant penetration of an incident acoustic field into sandy sediments below the critical grazing angle  $\theta_c = \cos^{-1}(1/\nu)$ . Subsequently, Jackson *et al.* [7] demonstrated that ripples are the primary surface feature needed to cause this increased penetration. Their model for the penetrating acoustic pressure,  $p$ , is expressed in a baseband representation, i.e., the signals are downshifted by the center frequency. In the present case the signal bandwidth is much greater, and therefore the baseband representation is not used, but otherwise the treatment here follows closely that given in [6]. Three possible contributions are contained in the model: a zeroth-order refracted field,

$p_R(\mathbf{r}, t)$ , a zeroth-order evanescent field,  $p_e(\mathbf{r}, t)$ , and a first-order surface (i.e., interface) scattered field,  $p_{2s}(\mathbf{r}, t)$ . Each field is briefly summarized below to unify the notation with the other models presented here as well as to absorb a  $1/4\pi$  scaling factor in (C15), (C21), and (C25) of [6] into the amplitude of the source waveform. This results in the same normalization for the reverberation and penetration models. (In [6] the source waveform normalization was taken to be the same as the point source Green's function as written in (C1) of [6], introducing a factor of  $1/4\pi$  in these equations.)

For a source located at  $\mathbf{r}_{src}$  and an in-sediment field point at  $\mathbf{r}_f$ , the refracted acoustic field is [6, see (C21)]

$$\begin{aligned} p_R(\mathbf{r}_f, t) = & r_0 \rho^{1/2} B_{src,R} \Gamma_{12E}(\theta_{iR}) p_{src}(t - t_R) \\ & \times [|\mathbf{R}_f - \mathbf{R}_{src}| \tan \theta_{2R} \sin \theta_{iR} \\ & \times (|z_{src}|/\sin^3 \theta_{iR} + \nu |z_f|/\sin^3 \theta_{2R})]^{-1/2} \end{aligned} \quad (4)$$

where the subscript  $R$  denotes quantities associated with the refracted path connecting the source at  $\mathbf{r}_{src}$  to the in-sediment field point at  $\mathbf{r}_f$ . For the refracted path,  $\theta_{iR}$  denotes the in-water grazing angle at the interface, and  $\theta_{2R}$  is the grazing angle of the refracted ray in the sediment (medium 2). The determination of  $\theta_{iR}$  will be described below, and  $\theta_{2R}$  is related to  $\theta_{iR}$  by Snell's law,  $\cos \theta_{2R} = \nu \cos \theta_{iR}$ , where the loss in the sediment is ignored in defining  $\theta_{2R}$ . The use of absolute values on the vertical coordinates ensures that (4) is invariant to the  $z$ -axis convention.  $B_{src,R}$  is the source response function evaluated at the refraction point, the point where the refracted path intersects the mean plane. The quantity  $\Gamma_{12E}(\theta_{iR})$  is a real transmission coefficient from medium 1 into medium 2 defined such that its square is the energy transmission coefficient. It is given by

$$\Gamma_{12E}(\theta_{iR}) = [1 - |\Gamma_{11}(\theta_{iR})|^2]^{1/2}, \quad (5)$$

where  $\Gamma_{11}(\theta_{iR})$  is given by (3). The parameter  $t_R = (d_{iR} + \kappa d_{2R})/c_1$  is a complex time delay where the imaginary part accounts for attenuation in the sediment. The distance from the source to the refraction point is  $d_{iR} = |z_{src}|/\sin \theta_{iR}$ , and  $d_{2R} = |z_f|/\sin \theta_{2R}$  is the distance from refraction point to the field point in the sediment.

To obtain  $\theta_{iR}$ , we begin by noting that the horizontal projections of the distances from the source to the refraction point and from the refraction point to the field point are given

by  $|z_{src}| \cot \theta_{iR}$  and  $|z_f| \cot \theta_{2R}$ , respectively. These must combine to give the total horizontal distance between the source and field point. Thus, we have

$$|\mathbf{R}_f - \mathbf{R}_{src}| = |z_{src}| \cot \theta_{iR} + |z_f| \cot \theta_{2R}. \quad (6)$$

It readily follows from (6) that

$$\begin{aligned} z_f^2 \cot^2 \theta_{2R} &= |\mathbf{R}_f - \mathbf{R}_{src}|^2 - 2|\mathbf{R}_f - \mathbf{R}_{src}||z_{src}| \\ &\quad \times \cot \theta_{iR} + z_{src}^2 \cot^2 \theta_{iR}. \end{aligned} \quad (7)$$

By using the identity

$$[1 + (1 - \nu^2) \cot^2 \theta_{iR}] \cot^2 \theta_{2R} = \nu^2 \cot^2 \theta_{iR}, \quad (8)$$

$\cot \theta_{2R}$  can be eliminated from (7) and the following quartic equation for  $\cot \theta_{iR}$  is obtained:

$$\sum_{j=0}^4 b_j \cot^j \theta_{iR} = 0, \quad (9)$$

where

$$\begin{aligned} b_0 &= |\mathbf{R}_f - \mathbf{R}_{src}|^2, & b_1 &= -2|\mathbf{R}_f - \mathbf{R}_{src}||z_{src}|, \\ b_2 &= z_{src}^2 + \mu|\mathbf{R}_f - \mathbf{R}_{src}|^2 - \nu^2 z_f^2, & & \\ b_3 &= -2\mu|\mathbf{R}_f - \mathbf{R}_{src}||z_{src}|, & b_4 &= \mu z_{src}^2, \end{aligned} \quad (10)$$

with  $\mu = 1 - \nu^2$ . Only the real, positive root of (9) is retained.

For the evanescent contribution, we define the incident grazing angle  $\theta_{ie}$  to be the grazing angle at the point on the interface directly above the field point in the sediment. (The subscript  $e$  denotes quantities associated with the evanescent field.) Thus,

$$\theta_{ie} = \sin^{-1}(|z_{src}|/d_{ie}), \quad (11)$$

where

$$d_{ie} = (|\mathbf{R}_f - \mathbf{R}_{src}|^2 + z_{src}^2)^{1/2} \quad (12)$$

is the distance from the source to the point  $(\mathbf{R}_f, 0)$  on the mean plane directly above the field point. As with the refracted field, the evanescent field is found for a flat interface making it a

zeroth-order contribution. If  $\theta_{ie}$  is greater than the critical angle, the evanescent contribution is set to zero. Otherwise, it takes the form [6, see (C25)]

$$p_e(\mathbf{r}_f, t) = r_0 B_{src,e} \Gamma_{12}(\theta_{ie}) p_{src}(t - t_e) / d_{ie}, \quad (13)$$

where  $B_{src,e}$  is the source response function evaluated at  $(\mathbf{R}_f, 0)$ . The plane-wave pressure transmission coefficient is

$$\Gamma_{12}(\theta_{ie}) = 1 + \Gamma_{11}(\theta_{ie}) = \frac{2\rho \sin \theta_{ie}}{\rho \sin \theta_{ie} + \kappa \sin \theta_{2e}} \quad (14)$$

where  $\theta_{2e}$  is a complex angle obtained from Snell's law with loss neglected; thus,

$$\sin \theta_{2e} = (1 - \nu^2 \cos^2 \theta_{ie})^{1/2}. \quad (15)$$

Note that when  $\theta_{ie}$  is less than the critical angle,  $\sin \theta_{2e}$  is purely imaginary. Finally, the complex time delay  $t_e$  is

$$t_e = (d_{ie} + \kappa d_{2e})/c_1 = (d_{ie} + \kappa |z_f| \sin \theta_{2e})/c_1. \quad (16)$$

Insertion of (16) into (13) reveals the characteristic exponential decay with depth into the sediment of an evanescent field. Thus,  $p_e(\mathbf{r}_f, t)$  is important only within a few wavelengths of the water-sediment interface.

The contribution to the penetrating acoustic field due to scattering from the rough surface is obtained with first-order perturbation theory, which gives

$$p_{2s}(\mathbf{r}_f, t) = \frac{\rho}{4\pi c_1^2} \int d^2 R \frac{A_s(\mathbf{R}) h(\mathbf{R}) \ddot{p}_{src}(t - t_s)}{|\mathbf{r}_f - \mathbf{R}| |\mathbf{R} - \mathbf{r}_{src}|}. \quad (17)$$

(See (C15) in [6] where  $-k_{10}^2 c_1^2 = -\omega_0^2$  has been replaced by the double time derivative applied to the source function.) The subscript  $s$  denotes a quantity associated with the scattered field, while the subscript  $2s$  indicates the scattered field is in the sediment (medium 2). The complex time delay is  $t_s = (d_i + \kappa d_{2s})/c_1$  where  $d_i = |\mathbf{R} - \mathbf{r}_{src}|$  and  $d_{2s} = |\mathbf{r}_f - \mathbf{R}|$ . The complex coefficient  $A_s(\mathbf{R})$  is given by

$$\begin{aligned} A_s(\mathbf{R}) &= r_0 B_{src} \Gamma_{12}(\theta_i) \Gamma_{21}(\theta_2) \left[ 1 - \frac{\kappa^2}{\rho} - \kappa \left( 1 - \frac{1}{\rho} \right) \right. \\ &\quad \times \left. \left( \frac{\mathbf{R}_f - \mathbf{R}}{d_{2s}} \cdot \frac{\mathbf{R} - \mathbf{R}_{src}}{d_i} + \sin \theta_{1s} \sin \theta_{2s} \right) \right] \end{aligned} \quad (18)$$

with the plane-wave pressure transmission coefficient from water into the sediment

$$\Gamma_{12}(\theta_i) = \frac{2\rho \sin \theta_i}{\rho \sin \theta_i + \kappa \sin \theta_{2s}}, \quad (19)$$

and the coefficient for transmission from the sediment into water

$$\Gamma_{21}(\theta_2) = \frac{2\kappa \sin \theta_2}{\kappa \sin \theta_2 + \rho \sin \theta_{1s}}. \quad (20)$$

From the specified geometry, the real grazing angles  $\theta_i$  and  $\theta_2$  satisfy  $\tan \theta_i = |z_{src}|/|\mathbf{R} - \mathbf{r}_{src}|$  and  $\tan \theta_2 = |z_f|/|\mathbf{r}_f - \mathbf{R}|$ , and the complex angles  $\theta_{2s}$  and  $\theta_{1s}$  are then determined from Snell's law:

$$\sin \theta_{2s} = (1 - \cos^2 \theta_i / \kappa^2)^{1/2}, \quad (21)$$

$$\sin \theta_{1s} = (1 - \kappa^2 \cos^2 \theta_2)^{1/2}. \quad (22)$$

### C. Target scattering

The steady-state interaction of an acoustic field with a finite target is modeled using the freefield scattering of an incident plane wave. At the ranges commonly found in SAS applications, the receiving transducer is in the far field of the target, and the scattered pressure for a freefield target can be written as

$$p_{tgt}(\mathbf{r}) = p_0 f(\hat{\mathbf{r}}, \hat{\mathbf{r}}_i) \exp(ikr)/r, \quad (23)$$

where  $p_0$  is the incident pressure at the target,  $f(\hat{\mathbf{r}}, \hat{\mathbf{r}}_i)$  is the scattering amplitude where  $\hat{\mathbf{r}}_i$  and  $\hat{\mathbf{r}}$  refer to the incident and scattering directions, respectively,  $r$  is the slant range from the target to the receiver, and  $k$  is the wavenumber in the water. As will be shown later in this section, scattering from a proud target can also be approximately put into the form of (23). The case of a buried target is more complicated, as discussed in Sec. III-C. The scattering amplitude also depends on frequency, but that dependence is suppressed. For SAS applications here we are interested only in monostatic backscatter, for which  $\hat{\mathbf{r}} = -\hat{\mathbf{r}}_i$ . Restricting the scattering amplitude to monostatic scattering allows it to be expressed using a single set of spherical angles  $f(\theta, \varphi)$ , where the coordinate origin is centered on the target. For a finite cylindrical target, we choose  $\theta$  to be the polar angle relative to the cylinder axis, and then by symmetry the scattering amplitude has no dependence on  $\varphi$ . For a spherical target, symmetry demands that there be no dependence on  $\theta$  or  $\varphi$ . In what follows the scattering amplitude is written as  $f(\theta)$ , which includes both cases.

It is convenient to express the scattering amplitude in terms of the dimensionless form function  $F(\theta)$ :

$$f(\theta) = \frac{a}{2} F(\theta), \quad (24)$$

where  $a$  is the radius of either a sphere or cylinder. The scattering cross section per unit solid angle is given by

$$\sigma = |f(\theta)|^2 = \frac{a^2}{4} |F(\theta)|^2 = \frac{\pi a^2}{4\pi} |F(\theta)|^2. \quad (25)$$

Thus, the form function can be viewed as an angular and frequency dependent correction to the scattering pattern of an ideal scatterer with total cross section  $\pi a^2$  that scatters uniformly over  $4\pi$  steradians. The target strength is given by  $TS = 10 \log_{10}(\sigma)$ .

Scattering for spheres and spherical shells is well understood and expressions for various form functions are readily available [8]–[11]. In particular, for a fluid-filled, elastic, spherical shell see Eq. (2) in [10].

Stanton considered broadside and near broadside scattering of sound from finite fluid and elastic cylinders [12], [13]. In the simulations of Sec. III, the axis of symmetry of the finite cylinder is parallel to the cross range axis. Stanton’s model was developed under the assumptions that end effects can be ignored and the length of the cylinder,  $L$ , satisfies  $L \ll 2\sqrt{r\lambda}$  and  $r \gg L$ , where  $\lambda$  is the wavelength of the incident acoustic field in the host medium. Stanton’s result can be cast into the following expression for the form function for backscattering from a finite cylinder:

$$F_{cyl}(\theta) = \frac{L}{a} \left( -\frac{\imath k_\perp a}{\pi} \right)^{1/2} \frac{\sin(k_\parallel L)}{k_\parallel L} F_\infty^{cyl}(k_\perp a), \quad (26)$$

where  $F_\infty^{cyl}(k_\perp a)$  is the form function for backscattering of a normally incident plane wave from an infinite cylinder. In (26) the perpendicular and parallel components of the wave vector are  $k_\perp = k \sin \theta$  and  $k_\parallel = k \cos \theta$ , respectively. The polar angle  $\theta$  is determined by  $\cos \theta = \hat{\mathbf{r}}_c \cdot \hat{\mathbf{r}}_{src}$ , where  $\hat{\mathbf{r}}_c$  is a unit vector parallel to the cylinder axis and  $\hat{\mathbf{r}}_{src}$  is a unit vector directed from the target center to the source position.

To obtain (26) first recall that scattering of a plane wave from an infinite cylinder is a two-dimensional problem, and therefore in place of (23) the scattered field is given by

$$p_{tgt}(\mathbf{r}) = p_0 f(\hat{\mathbf{r}}, \hat{\mathbf{r}}_i) \exp(\imath kr)/r^{1/2}. \quad (27)$$

For backscattering from an infinite circular cylinder, the scattering amplitude has no angular dependence, and here is represented in terms of its frequency dependence as  $f_\infty^{cyl}(k_\perp a)$ . (When expressed in terms of wavenumbers, the full dependence includes the compressional and shear wavenumbers in the elastic cylinder, but that dependence is suppressed.) An expression for

$f_\infty^{cyl}(k_\perp a)$  follows from Eq. (13) in [13] when specialized to backscattering. By convention [14] the dimensionless form function for scattering in a 2-D geometry is related to the scattering amplitude by  $F_\infty^{cyl}(k_\perp a) = (2/a)^{1/2} f_\infty^{cyl}(k_\perp a)$ . By using this relation and (24) plus Stanton's expressions for the scattering amplitudes for both finite and infinite length cylinders, (26) readily follows.

Ye revisited Stanton's model and provided a scattering amplitude that includes the scattering from a flat end [15]. His model was developed from a Kirchhoff scattering integral, which in the backscattering direction, reduces to (26) along the body of the finite cylinder. The backscattering contribution from a flat end is found to be

$$\begin{aligned} F_{end}(\theta, ka) &= -i\Gamma_{11}(\pi/2 - \theta) J_1(2ka \sin \theta) \cot \theta \\ &\quad \times \exp(-ikL \cos \theta), \end{aligned} \quad (28)$$

where an explicit dependence on  $ka$  is shown to aid discussion in Sec. III-B.  $\Gamma_{11}$  is the reflection coefficient for the interface between the water and the flat end,  $J_1$  is the first-order cylindrical Bessel function, and  $\theta$  is the angle that the incident wave vector makes with the cylinder axis. (The exponent sign and the overall sign given in [15] have been corrected in (28).) Because our present use of  $F_{end}(\theta, ka)$  is for incidence near end-on, we use for simplicity a reflection coefficient in the form of (3) but with the material parameters of the cylinder and the surrounding water; this neglects effects of shear in the reflection coefficient.

Scattering from proud targets is more difficult to model due to the interaction of the sound field with the target and bottom, including the possibility of multiple scattering. For this case we have used a simplified treatment in which the interaction of the incident sound field with the water-sediment interface and the target is modeled from a simple geometric ray analysis [5, See Fig. 5]. The ray diagrams for a sphere and cylinder at broadside incidence are identical, and yield an approximate backscattering form function

$$\begin{aligned} F(\theta_i) &= \Gamma_{tgt}(\pi/2) \exp(-i2ka) \\ &\quad + 2\Gamma_{tgt}(\pi/2 - \theta_i)\Gamma_{11}(\theta_i) \exp[i2ka(\sin \theta_i - \cos \theta_i)] \\ &\quad + \Gamma_{tgt}(\pi/2)\Gamma_{11}^2(\theta_i) \exp[i2ka(2 \sin \theta_i - 1)], \end{aligned} \quad (29)$$

where  $\theta_i$  is the incident grazing angle relative to the sediment surface. The form function given by (29) can be obtained using the Kirchhoff approximation for scattering followed by a stationary

phase analysis, consistent with a geometric ray analysis. (See Baik and Marston [16] and their Appendices I and II; these authors treat an analogous problem of a rigid cylinder near an interface and is a more general treatment than required here in that the cylinder can intersect the surface.) The water-sediment reflection coefficient,  $\Gamma_{11}(\theta_i)$ , is given by (3), and  $\Gamma_{tgt}$  is also evaluated from (3) using material properties of the target for the second medium. The first term in (29) is the field specularly backscattered from the target. The second term represents a ray that reflects from the water-sediment interface and is then specularly scattered by the target back to the source/receiver. This term also includes the reciprocal path of first specularly scattering from the target and then reflecting from the water-sediment interface. The last term accounts for a surface reflected ray that specularly backscatters from the target and then follows its incoming path back to the source/receiver. With direct substitution of (29) into (24), the approximate scattering from a proud spherical target is given by (23). Substitution of  $F(\theta_i)$  from (29) for  $F_\infty^{cyl}(k_\perp a)$  in (26) yields an approximation for scattering from a proud cylindrical target at and near a broadside orientation. In this expression  $\theta_i$  is again the incident grazing angle relative to the sediment surface, while  $\theta$  is the angle the incident wave vector makes with the cylinder axis.

Equation (29) includes only geometrically reflected ray paths and neglects possible surface guided waves contributions to the scattered field (e.g., leaky Rayleigh [5] or Lamb waves [11]). It is possible, however, to include the most important elastic effects by inserting more general form functions into each of the terms in (29). The first step is to re-express each term of (29) in terms of the form function for scattering from a sphere or cylinder based on geometric reflection only. To do this we must relax our earlier restriction to only monostatic scattering, since the second term in (29) corresponds to a vertical bistatic scattering combined with a reflection from the water-sediment interface. This extension of the formalism will at first be restricted here to the case of a spherical target. Thus, we write the form function for a spherical target as  $F_{sph}(\phi)$ , where  $\phi$  is the vertical angle for bistatic backscatter, defined such that  $\phi = \pi$  for monostatic backscatter. In particular, for scattering based on geometric reflection (i.e., reflection in the high frequency limit) one obtains  $F_{sph}(\phi) = \Gamma_{tgt}(\phi/2) \exp\{-i2ka \cos[(\pi - \phi)/2]\}$ . The phase factor accounts for the difference in path length between a path for scattering from a point at the center of the sphere and the path that reflects from the surface of the sphere. [An equivalent phase factor is given in [17] for the case of a rigid sphere, Eq. (10.103). Note that (29) corresponds to using just the leading term in Eq. (10.103) for the spherical target form function.] For the

geometry of a proud sphere,  $\phi = \pi$  in the first and third terms in (29) and  $\phi = \pi - 2\theta_i$  in the second term. Thus (29) becomes

$$\begin{aligned} F_p(\theta_i) &= F_{sph}(\pi) + 2\Gamma_{11}(\theta_i)F_{sph}(\pi - 2\theta_i)\exp(i2ka\sin\theta_i) \\ &\quad + \Gamma_{11}^2(\theta_i)F_{sph}(\pi)\exp(i4ka\sin\theta_i). \end{aligned} \quad (30)$$

The phase factors that survive in (30) arise from the path length differences for the terms in (29) when the target is considered a point. The form factors in (30) can now be generalized to approximately account for the most importance surface guided wave contributions. This was done by summing the partial wave series for scattering from an elastic spherical shell as given by Eq. (3) in [18], where the series was truncated using the second condition given in Eq. (16) in [18] for all  $ka$ . The partial wave series gives a more complete description of the specular reflection component than given by (29), and also includes the contribution of surface guided waves. The latter contribution may be overestimated because the effects of the sediment-target contact are not being taken into account.

The final piece of the target simulation is a Fourier synthesis to generate a scattered acoustic pulse emanating from the target location; this is necessary to account for the frequency dependence of the target's form function. Zhang *et al.* [19] provide a detailed description of a procedure similar to one outlined here. The complex pressure, after propagation from the source to the target location in the absence of the target, is convolved with the relevant form function. This is a three step process. First, the complex pressure is Fourier transformed into the frequency domain. Second, the form function as a function of angular frequency,  $F(\theta, \omega)$ , is computed for each of the positive frequencies of the complex signal, and the negative frequencies are populated by  $F(\theta; -\omega) = F^*(\theta; \omega)$  where  $*$  denotes complex conjugation. Third, the scattered signal is given by an inverse Fourier transform of the product of the form function and the Fourier transform of the complex signal.

### III. NUMERICAL SIMULATIONS AND COMPARISONS TO EXPERIMENTS

Several numerical simulations were conducted to validate individual models described in Sec. II, and some of those results are reported here. The simplest simulations are the freefield scattering from targets. These permit validation of the target models and the time domain imaging (TDI) algorithm described in Appendix II. Proud targets are then considered, which introduces

the interaction of the SAS signals with both the water-sediment interface and target. These simulations are compared to SAX04 data and data collected in the Naval Surface Warfare Center, Panama City Division (NSWC PCD) test pond facility. The simulations culminate with the imaging of buried targets under various conditions that correspond to SAX04 measurements.

Unless otherwise specified, the simulated data are sampled at 400 kHz and the time ranges from 0 to 24 ms. The length of the SAS aperture is typically 10 m and 400 individual signals are generated. This gives a spatial sampling of  $\Delta y = 0.025$  m, which is consistent with the  $\Delta y$  used during the experiments.

### A. Freefield scattering

For the freefield simulations, a source and a receiver are co-located, and initially placed at  $\mathbf{r}_{src} = (0, -5, 0)$  m. Omnidirectional beam patterns are used (i.e.,  $B_{src} = 1$  and  $B_{rcv} = 1$ ). A rigid sphere or rigid finite cylinder with broadside orientation is placed at  $\mathbf{r}_{tgt} = (10, 0, 0)$  m where the radii are  $a = 0.21$  m and the length of the cylinder is  $L = 1.1$  m. The target is in lossless water with  $c_1 = 1482$  m/s and  $\rho_1 = 1000$  kg/m<sup>3</sup>, which correspond to the water at the NSWC PCD test pond facility [20], [21].

The form of the chirp signal emitted by the source is given in (I.2). The carrier frequency is  $f_0 = 20$  kHz with a bandwidth of  $f_b = 15$  kHz and chirp duration of  $t_c = 3$  ms. The envelope parameter,  $a_c = 8$ , produces an effective bandwidth of  $f_{be} \approx 4.5$  kHz as determined from the full width at half maximum of the Fourier spectrum of the source replica. Throughout the simulations, a unit amplitude is assumed. A set of SAS signals are now generated by time shifting the replica to account for propagation from  $\mathbf{r}_{src}$  to  $\mathbf{r}_{tgt}$  and scaling by the geometric spreading, performing the convolution described in Sec. II-C, and finally time shifting the scattered signal from  $\mathbf{r}_{tgt}$  to  $\mathbf{r}_{rcv}$  and again including the geometric spreading.

The target strength of a sphere, as given by Urick [22], is  $TS_s = 10 \log_{10}(a^2/4)$ , which yields  $TS_s = -19.58$  dB. To determine a target strength from Fig. 1a, it is noted that TDI compensates for the spherical spreading for propagation from the source to each point in the image. The distance of closest approach to the center of the rigid sphere is  $R_d = 10$  m giving a one-way spreading loss of  $-20.00$  dB that needs to be removed. Additionally, all signals in the SAS aperture contribute to the image formation, so the image needs to be adjusted by  $-20 \log_{10} 400 = -52.04$  dB. The “hottest” pixel in Fig. 1a corresponds to 12.63 dB. Thus, we

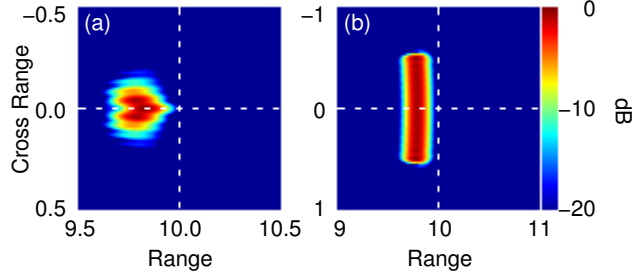


Fig. 1. SAS images of the freefield scattering from (a) a rigid sphere and (b) a finite rigid cylinder. The color scale is referenced to 12.63 dB and 11.42 dB for (a) and (b), respectively.

find  $TS_s^i = 12.63 - 52.04 + 20.00 = -19.41$  dB, which compares favorably with Urick's value.

From Urick, the target strength of a finite cylinder at broadside, is  $TS_c = 10 \log_{10}(aL^2/2\lambda)$ , and yields  $TS_c = 2.34$  dB at 20 kHz. To determine a target strength from Fig. 1b, the one-way spreading loss of  $-20.00$  dB again needs to be removed to account for the propagation from  $\mathbf{r}_{tgt}$  to  $\mathbf{r}_{rcv}$ . The number of SAS signals that actively contribute to an image is not governed by the length of the SAS aperture, but rather by the full width of the main lobe of the finite cylinder's directivity pattern. From Kinsler *et al.* [23], the main lobe for a rectangular aperture goes as  $\sin^2 v/v^2$  with  $v = kL \sin \theta/2$  and  $\theta$  is the angle between the axis that is perpendicular to the cylinder's axis of symmetry and the ray from the origin to the field point. For the simulation depicted in Fig. 1b, the half-width angle is  $\theta_h = 1.7^\circ$ . The number of signals contained within the half width of the main lobe is given by  $\tan \theta_h = n\Delta y/R_d \approx \theta_h$  with again a distance of closest approach denoted by  $R_d$ . The total number of contributing signals is then  $N = 2n \approx 2\theta_h R_d / \Delta y = 23.74$ . To estimate the target strength from Fig. 1b, the averaged squared pixel value over the "hottest" portion of the image is found, and it gives  $10 \log_{10}\langle P^2 \rangle = 9.08$  dB. The estimated target strength is now  $TS_c^i = 9.08 - 27.51 + 20.00 = 1.57$ , which is again in good agreement with Urick. It is noted that a value of  $N = 21.7$  reproduces  $TS_c$ .

The final freefield simulation is a cement drainage pipe with an end-on orientation. The relevant water parameters from SAX04 are  $c_1 = 1538$  m/s and  $\rho_1 = 1000$  kg/m<sup>3</sup>. For the pipe, the compressional sound speed and density of the cement are taken to be  $c_3 = 3100$  m/s and  $\rho_3 = 2600$  kg/m<sup>3</sup>, and the shear properties are ignored. The outer radius of the pipe is  $a = 0.21$  m and the ratio of the inner-to-outer radii is  $b/a = 0.819$ . To facilitate comparison to the SAX04 measurement, the initial source and receiver locations are  $\mathbf{r}_{src} = (0, -5, 3.86)$

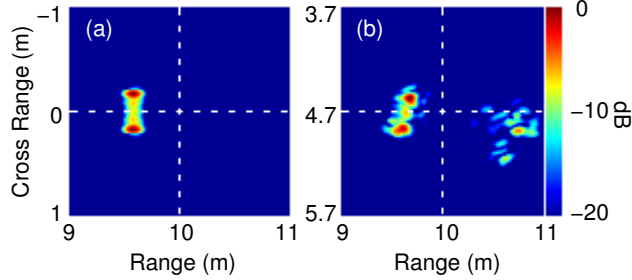


Fig. 2. SAS images of the freefield scattering from (a) a cement drainage pipe with an end-on orientation and (b) a proud cement pipe during SAX04.

$\mathbf{m}$  and  $\mathbf{r}_{rcv} = (0, -5, 3.91)$  m such that  $z_{src}$  and  $z_{rcv}$  are the nominal measured values from the mean sediment surface to the center of the aperture. The center of the pipe is located at  $\mathbf{r}_{tgt} = (10.25, 0, 0.21)$  m. The simulation constructs the required scattering form function from two applications of (28),  $F = F_{end}(\theta, k_1 a) - F_{end}(\theta, k_1 b)$ . The bandwidth and duration of the chirp have been increased to  $f_b = 25$  kHz and  $t_c = 4$  ms while  $a_c = 8$  is retained. This gives an effective bandwidth of  $f_{be} \approx 7.5$  kHz, which is consistent with the bandwidth of the SAX04 12–28 kHz chirp. The simulation is depicted in Fig. 2a where the result clearly shows the two glints observed in the SAX04 data shown in Fig. 2b. [The geometry for the SAX04 measurement actually had the target proud on the sediment, but the important observation is that the characteristic signature of the target shown in the simulation is evident in the measurement.] Additionally, the separation distance between glints are consistent with the observed glints. Figure 2b also shows glints at the far end of pipe. The simulation does not currently take into account the propagation along the pipe nor the scattering from the far end in the end-on orientation.

### B. Proud target

These simulations use the scattering amplitude given by (29) and (30). A few comments are in order. First, (29) only includes geometrically scattered contributions to the pressure, which obviously excludes possible resonant or elastic target responses. These contributions are included in (30). Second, the simulations also exclude a surface reverberation component because the observed SNR is greater than 25 dB. Third, a set of signals for SAS processing is generated in a manner similar to the method described in Sec. III-A. That is, a chirp is time shifted to the target location and scaled by the propagation distance, convolved with the scattering amplitude,

and then time shifted to the receiver. The following describes simulations and experiments for scattering from a proud spherical target in the NSWC PCD test pond facility and a cement drainage pipe at broadside incidence during SAX04.

Figure 3 depicts SAS images, generated from simulated and experimental data, for the scattering from an air-filled, proud, elastic spherical shell. The shell has an outer radius of  $a = 0.3$  m and an inner-to-outer radii ratio of  $b/a = 0.95$ . The shell's material was a mild steel. The SAS aperture for the measurement includes 764 pings, which gives a 19.1 m length aperture. The center of the physical apertures in the experiment were initially located at  $\mathbf{r}_{src} \approx (0, -10.25, 3.86)$  m and  $\mathbf{r}_{rcv} \approx (0, -9.76, 3.89)$  m. In the simulation, the initial source, initial receiver, and target locations are  $\mathbf{r}_{src} = (0, -5, 3.86)$  m,  $\mathbf{r}_{rcv} = (0, -5, 3.89)$  m, and  $\mathbf{r}_{tgt} = (9.35, 0.25, 0.3)$  m, respectively. The apertures are directed toward the sediment at a 20° depression angle with source and receiver dimensions of  $0.1 \times 0.05$  and  $0.1 \times 0.1$  m<sup>2</sup>. The chirp, used in the simulations, has a carrier frequency of  $f_0 = 20$  kHz with a bandwidth of  $f_b = 28$  kHz, duration of  $t_c = 4$  ms, and envelope parameter of  $a_c = 8$ . This yields an effective bandwidth of  $f_{be} \approx 15.4$  kHz, and the sample rate is 1 MHz. The density and sound speed of the test pond water are given in Sec. III-A. Finally, for completeness, the density, compressional speed, and shear speed of the mild steel are  $\rho_3 = 7700$  kg/m<sup>3</sup>,  $c_{l3} = 5950$  m/s, and  $c_{s3} = 3240$  m/s.

Figures 3a and b are SAS images created from simulated data sets with the form functions given in (29) and (30). In (30), we used the form function for an air-filled, elastic spherical shell for  $F_{sph}(\pi)$  and  $F_{sph}(\pi - 2\theta_i)$ . Figure 3c is the SAS image from experimental data. The three leftmost features in these images can be uniquely identified with the geometrically reflected ray contributions contained in (29). In Fig. 3a and b, the spatial separation between the left and center features is 0.13 m and the spatial separation between the center and right features is 0.10 m. For the experimental data, these features have spatial separations of 0.085 and 0.095 m, respectively. In the simulations, the target is assumed to be in contact with the water-sediment interface at a tangent point. In the experiment, the target's weight slightly depresses the interface and, hence, shortens the ray paths that interact with the interface. Inspection of Fig. 3b and c also reveals a feature near a range of 10 m. This feature is associated with the subsonic branch of the lowest order antisymmetric leaky Lamb wave, which is often designated as the  $A_{0-}$  leaky Lamb wave [19].

The proud target simulation in Fig. 4 approximates a broadside measurement from a cement

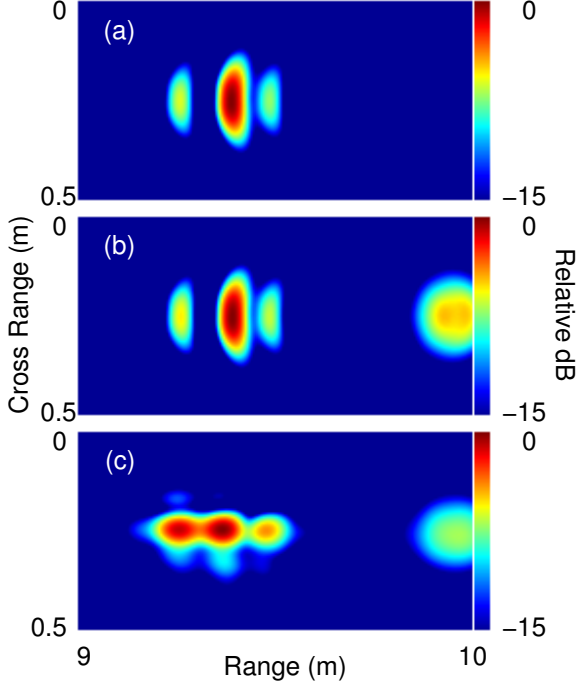


Fig. 3. SAS images of a proud elastic spherical shell. (a) The scattering model used (29) to generate data. This simulation includes only the geometrically reflected acoustic field. (b) The scattering model used (30), which includes both the reflected acoustic field and the elastic response of the shell. (c) SAS image generated from a measurement at the NSWC PCD test pond facility.

drainage pipe during SAX04. The environmental parameters are those given above for the end-on orientation of the pipe with the additional SAX04 sediment properties:  $\rho_2 = 2000 \text{ kg/m}^3$ ,  $c_2 = 1779 \text{ m/s}$ , and  $\delta_2 = 0.01$ . The center of the pipe is now at  $\mathbf{r}_{tgt} = (9.8, 0, 0.21) \text{ m}$ , and its length is nominally  $L = 1.09 \text{ m}$ . The locations and physical properties of the source and receiver are the same as those used in the proud spherical shell measurement. For this simulation the form function will again be generalized to include the most important elastic effects using an expression similar to (30). This requires including two angles in the finite cylinder form function now denoted  $F_{cyl}(\theta, \phi)$ , where  $\theta$  is the same polar angle used in (26), and  $\phi$  is the vertical bistatic angle. The form function given by (26) is for monostatic backscatter. In the generalization to include vertical bistatic scattering and elastic effects the only change required is to replace the final factor by  $F_{\infty}^{cyl}(k_{\perp}a, \phi)$ , corresponding to vertical bistatic scattering from a water-filled, elastic, infinite cylindrical shell [12]. The simulation uses (30) with the spherical shell form factors replaced by  $F_{cyl}(\theta, \pi)$  and  $F_{cyl}(\theta, \pi - 2\theta_i)$ . At the extreme ends of the SAS

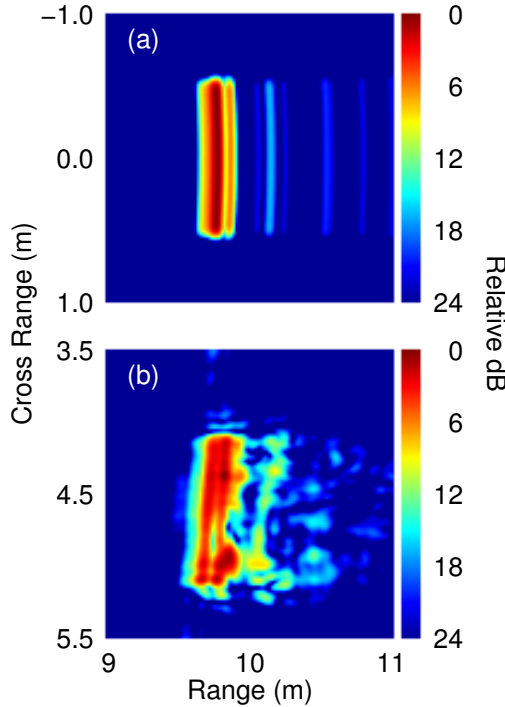


Fig. 4. SAS images of the scattering from a proud cement drainage pipe with a broadside orientation: (a) simulation and (b) SAX04 measurement.

aperture, the incident angle is nominally  $26^\circ$  from broadside and one may anticipate a failure in (30) due to (26). However, the discussion of the freefield image of the finite rigid cylinder shown in Fig. 1b suggests that only the central  $\sim 20$  signals contribute significantly to the image. The extreme angle of incidence for the signals of consequence is  $\sim 1.5^\circ$ , and hence, (30) with (26) should be adequate. Inspection of Fig. 4 shows that the simulation captures not only the length and width of the target, but also a “doublet”. This splitting is a clear indication of the interaction of the target scattering with the sediment interface as characterized by the ray model in Sec. II-C. Finally, the broad light blue feature at an approximate 10.2 m range suggests that an elastic response of the pipe has been stimulated (such as a surface elastic wave).

### C. Buried targets

The buried target simulations require three basic steps: (1) generate a realization of the rough seafloor; (2) compute reverberation from the seafloor; and, (3) compute a signal scattered from the target. Each step is briefly outlined below.

A realization of a seafloor must be generated in accordance with measured small-scale roughness and ripple structure. The small-scale roughness spectrum is given as an isotropic power law with an algebraic cut-off

$$W(k_x, k_y) = w_2/(k_s^2 + k_c^2)^{\gamma_2/2} \quad (31)$$

where  $k_x$  and  $k_y$  are the Cartesian components of the spatial wavenumber,  $k_s^2 = k_x^2 + k_y^2$ , and a constant cut-off typically taken to be  $k_c = 20.9 \text{ m}^{-1}$  (i.e., a 0.3 m length scale). Fourier methods can be used to convert  $W(k_x, k_y)$  into a small-scale surface relief. The general form of a sine-wave ripple is given by Jackson [7, see (1) and (2)], and its importance to acoustic penetration is discussed therein. For simulations, the ripple crests are parallel to the cross range direction.

Reverberation is computed from (1) with a surface realization that is “sufficiently large” to accommodate all positions along the SAS aperture, the typically wide horizontal beamwidths of the source and receiver, and the total duration of a signal [24]. The surface integral is converted to discrete sums over the mean surface coordinate  $\mathbf{R}_{ij} = (x_i, y_j)$  such that

$$p_{rev}(t_n) = \frac{\Delta x \Delta y}{4\pi c_1^2} \sum_{i=0}^{N_x} \sum_{j=0}^{N_y} \frac{A_{rev}^{ij} h_{ij}}{r_{rcv}^{ij} r_{src}^{ij}} \ddot{p}_{src}(t_n - t_{rev}^{ij}) \quad (32)$$

where  $r_{rcv}^{ij} = |\mathbf{r}_{rcv} - \mathbf{R}_{ij}|$ ,  $r_{src}^{ij} = |\mathbf{R}_{ij} - \mathbf{r}_{src}|$ ,  $A_{rev}^{ij} = A_{rev}(\mathbf{R}_{ij})$ ,  $t_{rev}^{ij} = (r_{src}^{ij} + r_{rcv}^{ij})/c_1$ ,  $\Delta x < c_1/[4(f_0 + f_b/2)]$  and similarly for  $\Delta y$ , and  $t_n = n\Delta t$  for  $n = 0, \dots, N_t$ . Direct evaluation of  $\ddot{p}_{src}(t_n - t_{rev}^{ij})$  for each discrete surface point and discrete round-trip delay time is possible, but numerically inefficient. To rapidly evaluate (32),  $\ddot{p}_{src}(t)$  is computed once at a much finer resolution  $\delta t \ll \Delta t$  in the interval  $0 \leq t \leq t_c$ . Outside of this interval,  $\ddot{p}_{src}(t)$  is identically zero. Then,  $\ddot{p}_{src}(t)$  is linearly interpolated onto  $p_{rev}(t_n)$  by time shifting  $\ddot{p}_{src}(t)$  to  $t_{rev}^{ij}$  with an appropriate scaling from the other factors in the summand.

The scattered target signal is computed in three steps. First, the refracted, evanescent, and surface scattered contributions in going from the source to the buried target location are determined from (4), (13), and (17), respectively. The surface integral in (17) is again reduced to a double summation over discrete points on the surface realization

$$p_{2s}(t_n) = \frac{\rho \Delta x \Delta y}{4\pi c_1^2} \sum_{i=0}^{M_x} \sum_{j=0}^{M_y} \frac{A_s^{ij} h_{ij}}{r_f^{ij} r_{src}^{ij}} \ddot{p}_{src}(t_n - t_s^{ij}), \quad (33)$$

with  $M_x \ll N_x$  and  $M_y \ll N_y$ . Only those points within a small area in the vicinity of target contribute. In (33),  $r_f^{ij} = |\mathbf{R}_{ij} - \mathbf{r}_f|$  is the distance from  $(x_i, y_j)$  to the field point. The method

used to rapidly evaluate (32) in general cannot be applied to (33) because  $t_s^{ij}$  is a complex time delay. However, for signals of the form given by (I.1)–(I.3), interpolation schemes can be implemented to account for  $t_s^{ij}$ .

The second step convolves the predicted penetrating signals with the target response as described in Sec. II-C. To investigate the importance of the refracted, evanescent, and surface scattered contributions, each is convolved with the target response independently.

The third step propagates the three scattered signals from the target to the receiver. To accomplish this step, the scattered signals are again propagated via (4), (13), and (17) with an appropriate change of coordinates for the source and field point locations. By tracking the individual paths back to the receiver, a total of nine possible signals are generated. For example, the acoustic energy refracted into the sediment scatters from the target and a portion of this scattered acoustic energy can arrive at the receiver via a refracted, evanescent, or surface scattering mechanism. Hence, the refracted-refracted signal is  $p_{RR}(t)$ , the refracted-evanescent signal is  $p_{RE}(t)$ , and the refracted-scattered signal is  $p_{R1}(t)$ . A final detail of the third step is a simple time shifting and interpolation scheme similar to the one used in the surface reverberation computation. This is required because the scattered signals no longer have an analytic form. In this step, only attenuation from the exponential factors in (4), (13), and (17) is included while the dispersion associated with the complex time delay is omitted.

In preparation for the SAX04 SAS measurements conducted during October 2004, proud and buried target fields were deployed during the Spring of 2004 off the coast of Fort Walton Beach, Florida. The intent of the early deployment was to allow natural scouring and benthic activity to heal any anthropogenic artifacts. Subsequent to the deployment and prior to the SAX04 field effort, several major weather events nearly destroyed the target fields. Fortunately, a few buried targets survived, and a focusing fluid sphere and cement drainage pipe were located from SAS measurements. For brevity, only images constructed from data sequence 16 (recorded on 2 October 04) and sequences 44 and 51 (recorded on 4 October 04) are analyzed here.

The APL-UW SAS system and the STMS2 electronics package have been described elsewhere [4], so only the operational parameters relevant to the SAS processing are given. An instrumented tower moved along the rail at a constant speed of 0.05 m/s, and it emitted 2 pings per second. Imposing the “stop-start” assumption [25], the spatial separation of adjacent pings is  $\Delta y = 0.025$  m. A typical sequence contains 1080 pings, which gives a 27 m SAS aperture. Each ping was

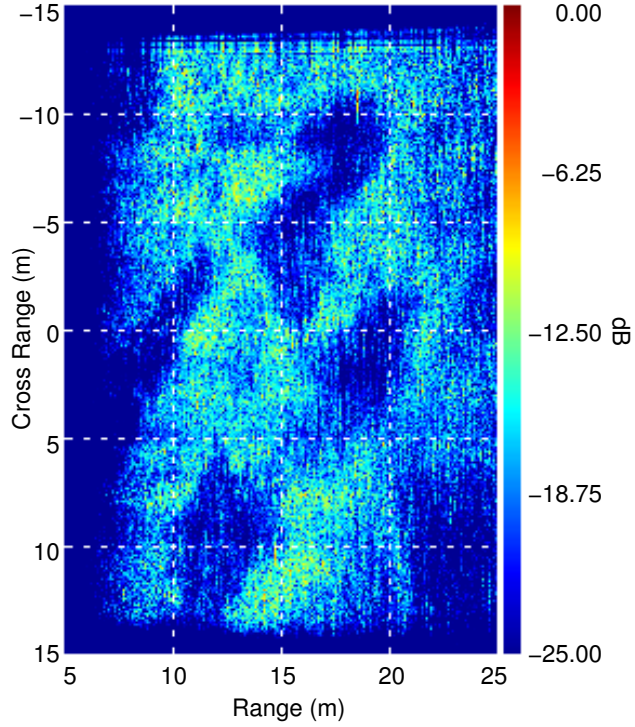


Fig. 5. SAS image of large area from sequence 44 of SAX04 data. The carrier frequency and bandwidth are  $f_0 = 150$  and  $f_b = 80$  kHz, respectively.

recorded for 200 ms at a 1 MHz sample rate.

Figure 5 displays the SAS image created from sequence 44. A 110–190 kHz chirp with a 4 ms duration was applied to the source. The source and receiver apertures are  $0.1 \times 0.02$  and  $0.1 \times 0.01$  m $^2$  where the leading dimension is the horizontal length. Both apertures are directed at the sediment interface at a  $20^\circ$  depression angle. The source and receiver elevations are 4.83 and 4.79 m above the mean sediment interface. Inspection of Fig. 5 shows regions of high and low backscatter. The regions of low backscatter have been correlated with a thin layer of mud on the sediment surface via diver observations. Furthermore, measurements of sediment profiles by Tang *et al.* [26] in nearby locations revealed distinct mud layers. Clearly, if a buried target were located beneath a mud patch, then the reduced backscatter would facilitate detection. Although not visible due to the frequency band, a buried focusing fluid sphere is detected at a lower frequency at approximately (10,10) m, which is near the edge of a mud patch.

The rough surface realization, used in the simulations to follow, was composed from two sine-

wave ripples and a small-scale isotropic roughness component for a water-sand interface. The ripple wavelengths were 0.75 and 0.44 m with RMS heights of 0.015 and 0.011 m, respectively. The phases of the ripples at  $x = 0$  were  $\phi_{75} = 0^\circ$  and  $\phi_{44} = 37^\circ$ . These ripples are consistent with profiles given by Tang *et al.* [26]. The small-scale roughness was generated from (31) with  $\gamma_2 = 5.29$  and  $w_2 = 1.597 \text{ m}^{4-\gamma_2}$ , which were obtained by Williams *et al.* [27] from measurements on a water-sand interface during SAX04. Numerically, the generated surface was  $60 \times 40 \text{ m}^2$  with the first dimension corresponding to range and the second to cross range. The spatial increments were  $\Delta x = \Delta y = 0.008 \text{ m}$ .

The sound speed and density of the water are given in Sec. III-A; while the sediment's sound speed, density, and loss parameter are provided in Sec. III-B. The sound speeds give a critical angle of  $30^\circ$ . The material properties of the cement drainage pipe are given in Sec. III-A. The focusing fluid sphere is a thin steel shell filled with a silicon oil. The density, compressional speed, and shear speed in the steel are  $\rho_3 = 7890 \text{ kg/m}^3$ ,  $c_{l3} = 5790 \text{ m/s}$  and  $c_{s3} = 3100 \text{ m/s}$ , respectively. The outer radius is  $a = 0.178 \text{ m}$  and the inner-to-outer radii ratio is  $b/a = 0.99$ . The properties of the silicon oil were selected to maximize the focusing when embedded in a sediment. The sound speed and density are  $c_4 = 1004 \text{ m/s}$  and  $\rho_4 = 800 \text{ kg/m}^3$ . The silicon oil is also given a small loss parameter of  $\delta_4 = 0.01$ , which effectively dampens the elastic response of the shell that is associated with its shear properties.

Figure 6a displays the SAS image created from sequence 16. The source signal is a 12–28 kHz chirp with a 4 ms duration. The source and receiver apertures are  $0.1 \times 0.05$  and  $0.1 \times 0.1 \text{ m}^2$ , and the depression angles are again at  $20^\circ$ . The source and receiver elevations were 3.86 and 3.91 m above the mean sediment interface, which corresponds to a nominal grazing angle of  $20^\circ$  at the sediment interface above the focusing fluid sphere. After the SAS data collection, divers probed the site with thin rods and estimated a burial depth of 0.86 m to the top of the shell. Figure 6b displays an image created from a simulation of 1080 pings based on the models presented here and our best estimate of the environmental conditions, where only a single rough surface realization was used. The SAS aperture in the simulation extended from -13.5 to 13.5 m and adjacent pings are 0.025 m apart. Each ping is 24 ms in duration. The center of the focusing fluid sphere was located at  $\mathbf{r}_{tgt} = (10, 0, -1.04) \text{ m}$  (i.e., the top of the shell is buried to a 0.86 m depth and located at a horizontal range of 10 m from the SAS track).

To achieve a comparable SNR in Fig. 6b to the observed SNR in Fig. 6a, the reverberation

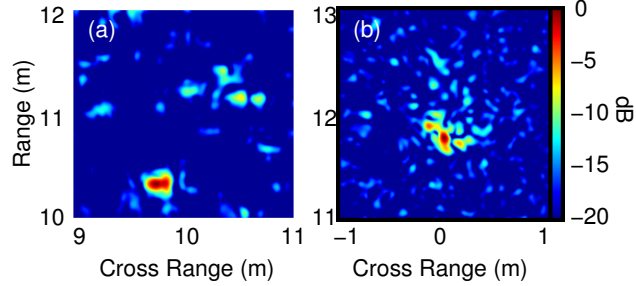


Fig. 6. SAS image of (a) a buried focusing fluid sphere from data sequence 16 taken during SAX04 (b) a numerical simulation.

predicted by (1) was reduced by a multiplicative factor of 0.18. At first glance, a 14.9 dB compensation may suggest that a problem exists within the simulation. However, inspection of Fig. 5 indicates that the overlying mud layer reduced reverberation by 6 to 8 dB relative to a region without mud. It is also noteworthy that roughness parameters, used in the generation of the small-scale surface roughness, are those for a sand-water not sand-mud interface. Additionally, the RMS heights of the ripples were estimated from surface profiles taken at nearby sites not at the location of the sphere. Diver observations elsewhere at the site and at later times found an estimated 0.07 m peak-to-trough ripple amplitude. This suggests that an increase in the RMS ripple heights could account for difference in the observed and simulated SNR. An increase of the RMS heights by a factor of 2 gives a 12 dB increase in the SNR.

The SAS image in Fig. 7 (left) is created from sequence 51. The source signal is a 12–28 kHz chirp with a 4 ms duration. The target is a cement drainage pipe in a nearly end-on orientation. The source and receiver elevations were 4.72 and 4.79 m above the mean water-sediment interface. With an observed horizontal range of 38.5 m to the target, the incident grazing angle above the pipe is approximately  $7^\circ$ , which is well below the critical grazing angle. The SAS image in Fig. 7 (right) is created from a simulation of an finite cylindrical pipe in an end-on orientation. As in Sec. III-A, the scattering amplitude is constructed from (28) via  $F = F_{end}(\theta, k_2a) - F_{end}(\theta, k_2b)$ . The center of the near end of the pipe was located at  $\mathbf{r}_{tgt} = (38, 0, -0.3)$  m. The initial source and receiver locations are  $\mathbf{r}_{src} = (0, -13.5, 4.72)$  m and  $\mathbf{r}_{rcv} = (0, -13.5, 4.79)$  m. Simulations generated 1080 pings with  $\Delta y = 0.025$  m, and each ping is 70 ms in duration.

To achieve a comparable SNR in Fig. 7 to the observed SNR, the simulated reverberation is

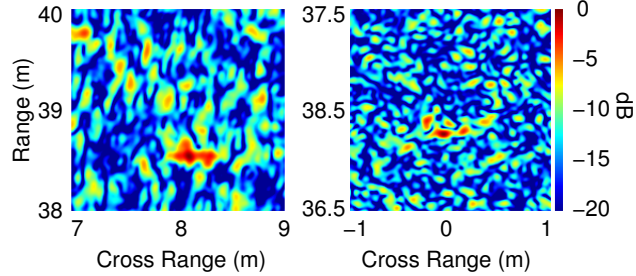


Fig. 7. Left: SAS image of a buried cement drainage pipe from data sequence 51 taken during SAX04. Right: numerical simulation.

reduced by a multiplicative factor of 0.14. Sequence 55 is a data set for a 110–190 kHz chirp, taken 2 hours after sequence 51. A  $10 \times 10 \text{ m}^2$  image, centered at  $\mathbf{R} = (38, 10) \text{ m}$  and generated from sequence 55, reveals that the observed target is near an edge, but outside, of a mud patch, and hence the 17 dB compensation cannot be attributed solely to reduced surface backscatter. Based on diver observations, it was argued that the RMS ripple heights could be increased (to account for the detection in Fig. 6a). However, a 17 dB compensation would require a factor of 2.75 increase (or an RMS height exceeding 0.04 m).

#### IV. CONCLUSION

Models for reverberation, acoustic penetration, and target scattering have been combined into a unified model in Sec. II. A salient feature of the unified model is its incorporation of the environment into a “single realization” modeling capability. The model can generate pings suitable for SAS simulations over a range of environmental (and experimental) conditions, which includes grazing angles below the sediment’s critical grazing angle. Model predictions can then be compared to experimental data to gain insight into the mechanisms important to proud and buried target detection. Section III discusses several simulations that validate the model against benchmark problems and experimentally measured target scattering from proud and buried targets.

Although this article concentrated on the scattering from spherical and finite cylindrical targets, the form of (23) permits other target shapes. If a target’s scattering response can be reduced to a form function  $F(\theta, \phi)$ , then it is straightforward to investigate the target’s potential appearance in SAS images. Methods for determining  $F(\theta, \phi)$  include the geometrical

theory of diffraction, numerical simulation via finite elements, and direct freefield experimental measurement. Obviously, the frequency response in any new form function would need to span the frequency band of the source signal.

Two refinements of the unified model are possible. First, the reverberation model in Sec. II-A is restricted to the backscattered direction. By removing this restriction, the current model would be applicable to bistatic SAS. Second, at fairly shallow grazing angles and a given ripple wavelength, a portion or even the entire frequency band of a chirp may exceed an inherent high-frequency cut-off via the ripple penetration mechanism. To accommodate this scenario, the penetration model would need to be updated. Two candidates are the addition of higher order terms from the perturbation theory that led to (17) or possibly a penetration model based on the small-slope approximation.

## APPENDIX I DERIVATION OF TIME-DOMAIN REVERBERATION MODEL

This appendix provides a derivation of (1), a time domain expression for the pressure field backscattered from roughness at the water-sediment interface where the sediment is considered as a homogeneous absorbing fluid. Several approximations are employed in obtaining (1): first-order perturbation theory is used for the treatment of scattering from roughness, the stationary phase approximation is used to evaluate the zero-order field where the frequency dependence of the source and receive beam patterns is neglected, the sound speed in the sediment is approximated as independent of frequency, and the attenuation in the sediment is approximated as linearly increasing with frequency. First-order perturbation theory yields the scattered field correct to first order in the small parameter  $k_1 h$ , where  $k_1$  is the wave number in the water, and  $h$  is the rms height of the interface roughness. The utility of making the final three approximations is that a time domain result can be obtained without the numerical effort inherent in a Fourier synthesis approach. The stationary phase approximation assumes the path lengths are large compared to the wavelength, a good approximation here. The assumption that the sediment sound speed is independent of frequency while the sediment attenuation increases linearly with frequency entails a negligible violation of causality [28]. The derivation will begin with the general bistatic case, and then specialize to the case where the source, receiver, and scattering patch lie in the same vertical plane, sufficient for the present applications.

Appendix C in [6] outlines the derivation of an analogous expression for scattering into the sediment, the primary penetration mechanism at low grazing angles, and the same approximations given above are used there. In addition, the relatively narrow bandwidths employed in [6] allowed the use of the baseband representation of the transmitted pulse with some simplifying approximations. For the present case the broadband linear chirp signal was emitted from the source at a center frequency of 20 kHz with a bandwidth of up to 16 kHz. A baseband representation could still be used, but the simplifying approximations made in [6] would not be appropriate. Instead, the baseband representation has simply been avoided in the present work.

We let  $p(\mathbf{r}, t)$  represent the space and time dependent pressure field. At unit distance from the source center on the transmit beam axis, we write the pressure as

$$p_{src}(t) = p_{src}s(t), \quad (\text{I.1})$$

where  $p_{src}$  is the maximum rms pressure of the source pulse (at pulse center) and where  $s(t)$  is the normalized pulse waveform with a maximum rms value of unity. (This representation anticipates the later stationary phase approximation, and uses the common expedient of defining a source waveform at unit distance as if near field effects can be ignored.) Specifically,

$$s(t) = \exp\{-a_c[(t - t_s)/t_s]^2\} \exp(i\phi), \quad (\text{I.2})$$

with

$$\phi = -\omega_0(t - t_s) - \pi K_c(t - t_s)^2. \quad (\text{I.3})$$

The pulse is initiated at  $t = 0$  and in (I.2) the constant  $a_c$  permits some control over the width of the Gaussian envelope independent of  $t_s$ . In (I.3)  $\omega_0 = 2\pi f_0$  with  $f_0$  the center frequency, and  $K_c$  is the chirp rate defined by  $K_c = f_b/t_c$  where  $f_b$  is the bandwidth and  $t_c = 2t_s$  is the duration of the chirp.

To obtain the time domain scattered pressure field we begin with a Fourier synthesis approach, and show later how that simplifies to the form given by (1) with the approximations mentioned at the beginning of this Appendix. First-order perturbation theory is used to obtain the scattered pressure field in the frequency domain, which is denoted by  $\psi_1^{(1)}(\mathbf{r}, \omega)$ , where the subscript 1 indicates a field in the water and the superscript (1) denotes first-order perturbation theory has

been used. The time-domain pressure field is then given by

$$p_1^{(1)}(\mathbf{r}, t) = \frac{1}{2\pi} \int_{-\infty}^{\infty} d\omega \psi_1^{(1)}(\mathbf{r}, \omega) S(\omega) \exp(-i\omega t), \quad (\text{I.4})$$

where

$$S(\omega) = \int_{-\infty}^{\infty} dt s(t) \exp(i\omega t). \quad (\text{I.5})$$

In order to obtain the necessary generality, a self-contained derivation will be outlined here for obtaining  $\psi_1^{(1)}(\mathbf{r}, \omega)$  and then the time-domain pressure field using (I.4). The derivation can be broken up into five steps: (1) Using the Helmholtz integral theorem to express the scattered field in terms of the fields just above and below the mean plane of the water-sediment interface and in terms of the Green's function for the case of a flat interface; (2) using perturbation theory and the boundary conditions to express the field quantities at the mean plane in terms of zero-order fields and  $h(\mathbf{R})$ , the rough water-sediment interface that varies with the horizontal coordinate  $\mathbf{R}$  (in this notation, the 3-D position vector  $\mathbf{r} = \mathbf{R} + z\hat{\mathbf{z}}$ ); (3) simplifying the resulting expression for  $\psi_1^{(1)}(\mathbf{r}, \omega)$  using integration by parts; (4) approximating the zero-order field and the Green's function using the stationary phase approximation; and (5) performing the  $\omega$  integration in (I.4) to get (1).

#### A. Getting started using the Helmholtz integral theorem

To state the problem, water above and sediment below (represented as a fluid) are separated by a rough interface defined by  $z = h(\mathbf{R})$  with the mean surface at  $z = 0$ . The  $z$ -axis is taken as directed upward from the mean plane into the water, and the coordinate system origin is taken as in the mean plane centered on a section of the rough interface of interest. The steady state, or CW, problem is considered at this point for a particular angular frequency  $\omega$ , but for simplicity of notation the  $\omega$  dependence will be suppressed until Sec. I-E. A general source distribution  $S_{src}(\mathbf{r})$  is assumed to reside entirely within the water (entirely above the highest point on the rough interface), and there are no sources in the sediment. Because the source may have spatial extent, a point source is not being assumed; in particular, the source may have arbitrary beam patterns. The pressure field in the water satisfies

$$\nabla^2 \psi_1(\mathbf{r}) + k_1^2 \psi_1(\mathbf{r}) = -S_{src}(\mathbf{r}). \quad (\text{I.6})$$

The subscript 1 will indicate quantities in the water and the subscript 2 will indicate quantities in the sediment. Thus,  $k_1 = \omega/c_1$  denotes the wave number in the water with  $c_1$  the water sound speed. The field  $\psi_2(\mathbf{r})$  that penetrates into the sediment satisfies

$$\nabla^2 \psi_2(\mathbf{r}) + k_2^2 \psi_2(\mathbf{r}) = 0, \quad (\text{I.7})$$

because there are no sources there. Also, the wave number  $k_2$  will be complex because of sediment absorption. The fields  $\psi_1(\mathbf{r})$  and  $\psi_2(\mathbf{r})$  satisfy the two-fluid boundary conditions on  $z = h(\mathbf{R})$ :

$$\psi_1(\mathbf{r})|_{z=h(\mathbf{R})} = \psi_2(\mathbf{r})|_{z=h(\mathbf{R})}, \quad (\text{I.8})$$

$$\frac{1}{\rho_1} \hat{\mathbf{n}} \cdot \nabla \psi_1(\mathbf{r})|_{z=h(\mathbf{R})^+} = \frac{1}{\rho_2} \hat{\mathbf{n}} \cdot \nabla \psi_2(\mathbf{r})|_{z=h(\mathbf{R})^-}, \quad (\text{I.9})$$

where  $\rho_1$  and  $\rho_2$  are the densities in the water and sediment, respectively, and where  $\hat{\mathbf{n}}$  is a unit vector normal to the surface  $h(\mathbf{R})$ .

Next let  $V_1$  and  $V_2$  be the volumes in the regions  $z > 0$  and  $z < 0$ , respectively, enclosed by the two hemispheres that are formed from a sphere bisected by the  $z = 0$  plane and centered horizontally on the origin. It is assumed that  $V_1$  entirely encloses the source distribution  $S_{src}(\mathbf{r})$ . Note that the hemisphere enclosing  $V_1$  is bounded from below by the  $z = 0$  plane, not the surface  $z = h(\mathbf{R})$ . This choice is essential for the development of perturbation theory. For any two fields  $\psi(\mathbf{r})$  and  $\phi(\mathbf{r})$  that satisfy the Helmholtz equation in  $V_1$ , the Helmholtz integral theorem relates the following volume integral over  $V_1$  to an integral over the surface  $S_1$  bounding  $V_1$ :

$$\begin{aligned} & \int_{V_1} dV' \{ \phi(\mathbf{r}') [\nabla'^2 \psi(\mathbf{r}') + k_1^2 \psi(\mathbf{r}')] \\ & \quad - \psi(\mathbf{r}') [\nabla'^2 \phi(\mathbf{r}') + k_1^2 \phi(\mathbf{r}')] \} \\ &= \int_{S_1} dS' [\phi(\mathbf{r}') \nabla' \psi(\mathbf{r}') - \psi(\mathbf{r}') \nabla' \phi(\mathbf{r}')] \cdot \hat{\mathbf{n}}', \end{aligned} \quad (\text{I.10})$$

where  $\hat{\mathbf{n}}'$  is the outwardly directed normal on  $S_1$  bounding  $V_1$ . In (I.10) we now let  $\psi(\mathbf{r}') \rightarrow \psi_1(\mathbf{r}')$  where we assume that when  $h(\mathbf{R}) > 0$ ,  $\psi_1(\mathbf{r}')$  can be defined in the region  $0 \leq z \leq h(\mathbf{R})$  by analytic continuation. Thus,  $\psi_1(\mathbf{r}')$  is defined throughout  $V_1$ . Also in (I.10) we let  $\phi(\mathbf{r}') \rightarrow G_1(\mathbf{r}', \mathbf{r})$ , the Green's function giving the field at  $\mathbf{r}'$ , which may be in  $V_1$  or  $V_2$ , due to a point source at  $\mathbf{r} \in V_1$  in the presence of a flat water-sediment interface at  $z = 0$ . This

Green's function is the solution to

$$\begin{aligned}\nabla'^2 G_1(\mathbf{r}', \mathbf{r}) + k_1^2 G_1(\mathbf{r}', \mathbf{r}) &= -\delta(\mathbf{r}' - \mathbf{r}), & \mathbf{r}' \in V_1, \\ \nabla'^2 G_1(\mathbf{r}', \mathbf{r}) + k_2^2 G_1(\mathbf{r}', \mathbf{r}) &= 0, & \mathbf{r}' \in V_2,\end{aligned}\quad (\text{I.11})$$

subject to the boundary conditions

$$G_1(\mathbf{r}', \mathbf{r})|_{z'=0^+} = G_1(\mathbf{r}', \mathbf{r})|_{z'=0^-} \quad (\text{I.12})$$

and

$$\frac{1}{\rho_1} \frac{\partial G_1(\mathbf{r}', \mathbf{r})}{\partial z'} \Big|_{z'=0^+} = \frac{1}{\rho_2} \frac{\partial G_1(\mathbf{r}', \mathbf{r})}{\partial z'} \Big|_{z'=0^-}. \quad (\text{I.13})$$

The surface  $S_1$  is that portion of the  $z = 0$  plane at the base of  $V_1$  plus the hemisphere above it. By the usual arguments for our choices for  $\psi(\mathbf{r})$  and  $\phi(\mathbf{r})$ , the integral over the hemispherical surface  $\rightarrow 0$  as its radius  $\rightarrow \infty$ . For this argument to carry through rigorously, it is convenient to assume that  $h(\mathbf{R})$  goes smoothly to zero when  $|\mathbf{R}|$  exceeds some small fraction of the hemisphere radius. Even so, as the hemisphere radius  $\rightarrow \infty$ , so does the radius of the region on the  $z = 0$  plane with roughness. We are left with just the surface integral over the  $z = 0$  plane, and in (I.10)  $\hat{\mathbf{n}}' = -\hat{\mathbf{z}}$ . Using (I.6) and (I.11) in (I.10) gives

$$\begin{aligned}\psi_1(\mathbf{r}) &= \int_{V_1} dV' S_{src}(\mathbf{r}') G_1(\mathbf{r}', \mathbf{r}) \\ &\quad - \int_{S_1} dS' \left[ G_1(\mathbf{r}', \mathbf{r}) \frac{\partial \psi_1(\mathbf{r}')}{\partial z'} \Big|_{z'=0^+} \right. \\ &\quad \left. - \psi_1(\mathbf{r}') \frac{\partial G_1(\mathbf{r}', \mathbf{r})}{\partial z'} \Big|_{z'=0^+} \right].\end{aligned}\quad (\text{I.14})$$

When both  $\mathbf{r}$  and  $\mathbf{r}'$  are in  $V_1$ , the reciprocity condition yields

$$G_1(\mathbf{r}', \mathbf{r}) = G_1(\mathbf{r}, \mathbf{r}'), \quad (\text{I.15})$$

which is then used in (I.14) to replace  $G_1(\mathbf{r}', \mathbf{r})$  with  $G_1(\mathbf{r}, \mathbf{r}')$ . We can identify the first term on the right hand side in (I.14) as the zero-order field in  $V_1$ :

$$\psi_1^{(0)}(\mathbf{r}) = \int_{V_1} dV' S_{src}(\mathbf{r}') G_1(\mathbf{r}, \mathbf{r}'). \quad (\text{I.16})$$

That is,  $\psi_1^{(0)}(\mathbf{r})$  is the solution in the absence of any roughness at the water-sediment interface and is made up of a direct component from the source and a component reflected from the

water-sediment interface. The scattered field is then given by

$$\begin{aligned} \psi_1(\mathbf{r}) - \psi_1^{(0)}(\mathbf{r}) = & - \int_{S_1} dS' \left[ G_1(\mathbf{r}, \mathbf{R}') \frac{\partial \psi_1(\mathbf{r}')}{\partial z'} \Big|_{z'=0^+} \right. \\ & \left. - \psi_1(\mathbf{R}') \frac{\partial G_1(\mathbf{r}, \mathbf{r}')}{\partial z'} \Big|_{z'=0^+} \right]. \end{aligned} \quad (\text{I.17})$$

It will be seen shortly that the right hand side of (I.17) indeed vanishes at zero order.

To proceed further the idea is to use first-order perturbation theory to express  $\psi_1$  and its  $z$ -derivative on  $S_1$  in terms of the zero-order field and the rough surface  $h(\mathbf{R})$ . The most convenient approach to this end is to first develop a second equation similar to (I.17) by use of the Helmholtz integral theorem in the volume  $V_2$  in the lower half plane. We then work with an equation similar to (I.10), the only differences being that  $k_1$  is replaced by  $k_2$ , the volume integral is over the volume  $V_2$  and the surface integral is over the surface  $S_2$  that encloses  $V_2$ . We then let  $\psi(\mathbf{r}') \rightarrow \psi_2(\mathbf{r}')$  where we assume that when  $h(\mathbf{R}) < 0$ ,  $\psi_2(\mathbf{r}')$  can be defined in the region  $h(\mathbf{R}) \leq z \leq 0$  by analytic continuation. Thus,  $\psi_2(\mathbf{r}')$  is defined throughout  $V_2$ . We also let  $\phi(\mathbf{r}') \rightarrow G_1(\mathbf{r}', \mathbf{r})$  as before, but now  $\mathbf{r}' \in V_2$  below the  $z = 0$  plane, while  $\mathbf{r} \in V_1$  above that plane. As before, as the radius of the hemisphere increases without bound, the integral over the hemispherical surface of  $S_2 \rightarrow 0$ . We are left with

$$\begin{aligned} 0 = & \int_{S_1} dS' \left[ G_1(\mathbf{r}', \mathbf{r})|_{z'=0^-} \frac{\partial \psi_2(\mathbf{r}')}{\partial z'} \Big|_{z'=0^-} \right. \\ & \left. - \psi_2(\mathbf{r}')|_{z'=0^-} \frac{\partial G_1(\mathbf{r}', \mathbf{r})}{\partial z'} \Big|_{z'=0^-} \right], \end{aligned} \quad (\text{I.18})$$

where the integration is now over the entire  $z = 0$  plane, the same as  $S_1$  in (I.17).

Terms corresponding to those on the left hand side in (I.17) do not appear in (I.18):  $\psi_2(\mathbf{r})$  because  $\delta(\mathbf{r}' - \mathbf{r})$  never acts in the integration over  $V_2$  and  $\psi_2^{(0)}(\mathbf{r})$  because there are no sources in  $V_2$ . There is a zero-order field in  $V_2$ , but it does not enter explicitly into (I.18). To prepare (I.18) for combining with (I.17), the Green's functions in (I.18) can be re-expressed using

$$G_1(\mathbf{r}', \mathbf{r})|_{z'=0^-} = G_1(\mathbf{r}', \mathbf{r})|_{z'=0^+} = G_1(\mathbf{r}, \mathbf{r}')|_{z'=0^+} \quad (\text{I.19})$$

and

$$\begin{aligned} \frac{\partial G_1(\mathbf{r}', \mathbf{r})}{\partial z'} \Big|_{z'=0^-} &= \frac{\rho_2}{\rho_1} \frac{\partial G_1(\mathbf{r}', \mathbf{r})}{\partial z'} \Big|_{z'=0^+} \\ &= \frac{\rho_2}{\rho_1} \frac{\partial G_1(\mathbf{r}, \mathbf{r}')}{\partial z'} \Big|_{z'=0^+} \end{aligned} \quad (\text{I.20})$$

In (I.19) and (I.20) the first equality follows from the boundary conditions (I.12) and (I.13), and the second equality follows from the reciprocity condition (I.15). Using (I.19) and (I.20) in (I.18) gives

$$0 = \int_{S_1} dS' \left[ G_1(\mathbf{r}, \mathbf{r}')|_{z'=0^+} \frac{\rho_1}{\rho_2} \frac{\partial \psi_2(\mathbf{r}')}{\partial z'} \Big|_{z'=0^-} - \psi_2(\mathbf{r}')|_{z'=0^-} \frac{\partial G_1(\mathbf{r}, \mathbf{r}')}{\partial z'} \Big|_{z'=0^+} \right], \quad (\text{I.21})$$

and adding (I.21) to (I.17) results in

$$\begin{aligned} & \psi_1(\mathbf{r}) - \psi_1^{(0)}(\mathbf{r}) \\ &= \int_{S_1} dS' \left\{ [\psi_1(\mathbf{R}') - \psi_2(\mathbf{R}')] \frac{\partial G_1(\mathbf{r}, \mathbf{r}')}{\partial z'} \Big|_{z'=0^+} \right. \\ &\quad - \left[ \frac{1}{\rho_1} \frac{\partial \psi_1(\mathbf{r}')}{\partial z'} \Big|_{z'=0^+} - \frac{1}{\rho_2} \frac{\partial \psi_2(\mathbf{r}')}{\partial z'} \Big|_{z'=0^-} \right] \\ &\quad \times \rho_1 G_1(\mathbf{r}, \mathbf{R}') \Big\}. \end{aligned} \quad (\text{I.22})$$

From (I.22) it is finally possible to see that the right hand side has no contribution to zero order ( $h(\mathbf{R}) = 0$ )), because for that case both expressions in brackets vanish by the boundary conditions (I.8) and (I.9). The result for the scattered field given by (I.22) is exact, except for the analytic continuation assumption. Perturbation theory has not been used.

### B. Introducing first-order perturbation theory

The first step in bringing in perturbation theory is to assume a perturbation expansion of the fields above and below the  $z = 0$  plane:

$$\psi_1(\mathbf{r}) = \psi_1^{(0)}(\mathbf{r}) + \psi_1^{(1)}(\mathbf{r}) + \dots, \quad (\text{I.23})$$

$$\psi_2(\mathbf{r}) = \psi_2^{(0)}(\mathbf{r}) + \psi_2^{(1)}(\mathbf{r}) + \dots \quad (\text{I.24})$$

where the zero-order fields denoted by the superscript (0) are the solutions when  $h(\mathbf{R}) = 0$ , and where the first-order fields denoted by the superscript (1) are the results correct to first-order in the perturbation theory expansion parameter  $k_1 h$ , where  $h$  is the rms value of  $h(\mathbf{R})$ . Thus, all higher-order terms will be dropped in the equations governing the first-order fields. We then

find from (I.22) that the first-order scattered field is given by

$$\begin{aligned} \psi_1^{(1)}(\mathbf{r}) = & \int_{S_1} dS' \left\{ [\psi_1^{(1)}(\mathbf{R}') - \psi_2^{(1)}(\mathbf{R}')] \frac{\partial G_1(\mathbf{r}, \mathbf{r}')}{\partial z'} \Big|_{z'=0^+} \right. \\ & - \left[ \frac{1}{\rho_1} \frac{\partial \psi_1^{(1)}(\mathbf{r}')}{\partial z'} \Big|_{z'=0^+} - \frac{1}{\rho_2} \frac{\partial \psi_2^{(1)}(\mathbf{r}')}{\partial z'} \Big|_{z'=0^-} \right] \\ & \left. \times \rho_1 G_1(\mathbf{r}, \mathbf{R}') \right\}. \end{aligned} \quad (\text{I.25})$$

To obtain an expression for the difference in the first set of brackets, the boundary condition (I.8) is expanded on both sides in a Taylor series about the mean plane, and collecting together all terms of first order yields

$$\begin{aligned} & \psi_1^{(1)}(\mathbf{R}) - \psi_2^{(1)}(\mathbf{R}) \\ &= h(\mathbf{R}) \left[ \frac{\partial \psi_2^{(0)}(\mathbf{r})}{\partial z} \Big|_{z=0^-} - \frac{\partial \psi_1^{(0)}(\mathbf{r})}{\partial z} \Big|_{z=0^+} \right]. \end{aligned} \quad (\text{I.26})$$

Then, the zero-order version of the boundary condition (I.9) can be used to eliminate  $\partial \psi_2^{(0)}(\mathbf{r})/\partial z|_{z=0^-}$  yielding

$$\begin{aligned} & \psi_1^{(1)}(\mathbf{R}) - \psi_2^{(1)}(\mathbf{R}) \\ &= h(\mathbf{R}) \left( \frac{\rho_2}{\rho_1} - 1 \right) \frac{\partial \psi_1^{(0)}(\mathbf{r})}{\partial z} \Big|_{z=0^+}. \end{aligned} \quad (\text{I.27})$$

For the difference in the second set of brackets, we begin with the boundary condition (I.9), use  $\hat{\mathbf{n}} = \mathbf{n}/|\mathbf{n}|$  with  $\mathbf{n} = -\nabla_{\perp} h(\mathbf{R}) + \hat{\mathbf{z}}$ , and rewrite (I.9) as

$$\begin{aligned} & \frac{1}{\rho_1} \left[ \frac{\partial \psi_1(\mathbf{r})}{\partial z} - \nabla_{\perp} h(\mathbf{R}) \cdot \nabla_{\perp} \psi_1(\mathbf{r}) \right] \Big|_{z=h(\mathbf{R})^+} \\ &= \frac{1}{\rho_2} \left[ \frac{\partial \psi_2(\mathbf{r})}{\partial z} - \nabla_{\perp} h(\mathbf{R}) \cdot \nabla_{\perp} \psi_2(\mathbf{r}) \right] \Big|_{z=h(\mathbf{R})^-} \end{aligned} \quad (\text{I.28})$$

where  $\nabla_{\perp}$  denotes the horizontal gradient operator (i.e.,  $\nabla = \nabla_{\perp} + \hat{\mathbf{z}}\partial/\partial z$ ). Expanding the

fields in a Taylor's series about the mean plane and collecting the first-order terms gives

$$\begin{aligned} & \frac{1}{\rho_1} \frac{\partial \psi_1^{(1)}(\mathbf{r})}{\partial z} \Big|_{z=0+} - \frac{1}{\rho_2} \frac{\partial \psi_2^{(1)}(\mathbf{r})}{\partial z} \Big|_{z=0-} = -h(\mathbf{R}) \\ & \times \left[ \frac{1}{\rho_1} \frac{\partial^2 \psi_1^{(0)}(\mathbf{r})}{\partial z^2} \Big|_{z=0+} - \frac{1}{\rho_2} \frac{\partial^2 \psi_2^{(0)}(\mathbf{r})}{\partial z^2} \Big|_{z=0-} \right] \\ & + \frac{1}{\rho_1} \nabla_{\perp} h(\mathbf{R}) \cdot \nabla_{\perp} \psi_1^{(0)}(\mathbf{r}) \Big|_{z=0+} \\ & - \frac{1}{\rho_2} \nabla_{\perp} h(\mathbf{R}) \cdot \nabla_{\perp} \psi_2^{(0)}(\mathbf{r}) \Big|_{z=0-}. \end{aligned} \quad (\text{I.29})$$

The second  $z$ -derivatives can be eliminated using (I.6) and (I.7), and then all terms on the right hand side involving  $\psi_2^{(0)}(\mathbf{r})$  can be re-expressed in terms of  $\psi_1^{(0)}(\mathbf{r})$  using the zero-order version of the boundary condition (I.8). The result is

$$\begin{aligned} & \frac{1}{\rho_1} \frac{\partial \psi_1^{(1)}(\mathbf{r})}{\partial z} \Big|_{z=0+} - \frac{1}{\rho_2} \frac{\partial \psi_2^{(1)}(\mathbf{r})}{\partial z} \Big|_{z=0-} = h(\mathbf{R}) \\ & \times \left[ \left( \frac{k_1^2}{\rho_1} - \frac{k_2^2}{\rho_2} \right) \psi_1^{(0)}(R) + \left( \frac{1}{\rho_1} - \frac{1}{\rho_2} \right) \nabla_{\perp}^2 \psi_1^{(0)}(\mathbf{R}) \right] \\ & + \left( \frac{1}{\rho_1} - \frac{1}{\rho_2} \right) \nabla_{\perp} h(\mathbf{R}) \cdot \nabla_{\perp} \psi_1^{(0)}(\mathbf{R}). \end{aligned} \quad (\text{I.30})$$

### C. Further simplification using integration by parts

When (I.27) and (I.30) are inserted in (I.25), there are terms linear in  $h(\mathbf{R})$  and one term linear in  $\nabla_{\perp} h(\mathbf{R})$ . In this section integration by parts is used to re-express the term in  $\nabla_{\perp} h(\mathbf{R})$  as a term in  $h(\mathbf{R})$ , which is a useful simplification. Let

$$\psi_1^{(1)}(\mathbf{r}) = \psi_{1A}^{(1)}(\mathbf{r}) + \psi_{1B}^{(1)}(\mathbf{r}), \quad (\text{I.31})$$

where  $\psi_{1A}^{(1)}(\mathbf{r})$  denotes the terms linear in  $h(\mathbf{R})$  and  $\psi_{1B}^{(1)}(\mathbf{r})$  denotes the term linear in  $\nabla_{\perp} h(\mathbf{R})$ .

Thus, we have

$$\begin{aligned} \psi_{1B}^{(1)}(\mathbf{r}) &= - \int_{S_1} dS' \left( \frac{1}{\rho_1} - \frac{1}{\rho_2} \right) \nabla'_{\perp} h(\mathbf{R}') \cdot \nabla'_{\perp} \psi_1^{(0)}(\mathbf{R}') \\ &\times \rho_1 G_1(\mathbf{r}, \mathbf{R}'). \end{aligned} \quad (\text{I.32})$$

Integrating (I.32) by parts leads to

$$\begin{aligned}\psi_{1B}^{(1)}(\mathbf{r}) &= \left( \frac{1}{\rho_1} - \frac{1}{\rho_2} \right) \rho_1 \\ &\times \int_{S_1} dS' h(\mathbf{R}') \{ [\nabla'_\perp \psi_1^{(0)}(\mathbf{R}')] G_1(\mathbf{r}, \mathbf{R}') \\ &+ \nabla'_\perp \psi_1^{(0)}(\mathbf{R}') \cdot \nabla'_\perp G_1(\mathbf{r}, \mathbf{R}') \}. \end{aligned} \quad (\text{I.33})$$

No boundary term appears after integration by parts because it has been assumed that  $h(\mathbf{R})$  vanishes well before the boundary is reached. (See discussion related to (I.14)). The first term in (I.33) cancels with the second term on the right hand side of (I.30) when it is inserted into (I.25). Collecting together the contributions to (I.25) gives

$$\begin{aligned}\psi_1^{(1)}(\mathbf{r}) &= \\ &- k_1^2 \int_{S_1} dS' h(\mathbf{R}') \left[ \left( 1 - \frac{\kappa^2}{\rho} \right) \psi_1^{(0)}(\mathbf{R}') G_1(\mathbf{r}, \mathbf{R}') \right. \\ &- \frac{\rho - 1}{k_1^2} \frac{\partial \psi_1^{(0)}(\mathbf{r}')}{\partial z'} \Big|_{z'=0^+} \frac{\partial G_1(\mathbf{r}, \mathbf{r}')}{\partial z'} \Big|_{z'=0^+} \\ &\left. - \frac{\rho - 1}{k_1^2 \rho} \nabla'_\perp \psi_1^{(0)}(\mathbf{R}') \cdot \nabla'_\perp G_1(\mathbf{r}, \mathbf{R}') \right], \end{aligned} \quad (\text{I.34})$$

where  $\kappa = k_2/k_1$  and  $\rho = \rho_2/\rho_1$ .

#### D. The stationary phase approximation

The expression given by (I.34) is valid for arbitrary zero-order fields, and can be written in terms of wave number integration over plane waves. If the stationary phase approximation is applied to such a representation, the zero-order field reduces to

$$\begin{aligned}\psi_1^{(0)}(\mathbf{r}) &= p_{src} r_0 \left[ B_{src}(\mathbf{r}, \mathbf{r}_{src}) \frac{\exp(i k_1 |\mathbf{r} - \mathbf{r}_{src}|)}{|\mathbf{r} - \mathbf{r}_{src}|} \right. \\ &\left. + B_{src}(\mathbf{r}, \mathbf{r}'_{src}) \Gamma_{11}(\mathbf{r}, \mathbf{r}_{src}) \frac{\exp(i k_1 |\mathbf{r} - \mathbf{r}'_{src}|)}{|\mathbf{r} - \mathbf{r}'_{src}|} \right], \end{aligned} \quad (\text{I.35})$$

where  $r_0 = 1$  m and  $B_{src}(\mathbf{r}, \mathbf{r}_{src})$  is the source response function at field point  $\mathbf{r}$  for the source at  $\mathbf{r}_{src}$ . (The beam pattern is the square of the response function.) Also,  $\mathbf{r}'_{src}$  is the location of the image source about the mean plane, and  $\Gamma_{11}(\mathbf{r}, \mathbf{r}_{src})$  is the reflection coefficient for a ray from  $\mathbf{r}_{src}$  to  $\mathbf{r}$  via a reflection from the mean plane. It follows from (I.35) that the zero-order

field on the mean plane is given by

$$\begin{aligned}\psi_1^{(0)}(\mathbf{R}') &= p_{src}r_0B_{src}(\mathbf{R}')[1 + \Gamma_{11}(\theta_i)] \\ &\times \frac{\exp(\imath k_1|\mathbf{R}' - \mathbf{r}_{src}|)}{|\mathbf{R}' - \mathbf{r}_{src}|},\end{aligned}\quad (\text{I.36})$$

where  $B_{src}(\mathbf{R}')$  is the source response function projected onto the mean plane, with the dependence of the source position suppressed, and where  $\Gamma_{11}(\theta_i)$  is the reflection coefficient re-expressed in terms of the grazing angle of the incident ray and is given by (3). (The 11 subscript indicates that the ingoing and outgoing rays are in medium 1.) The stationary phase approximation assumes the path lengths are large compared to the wavelength, a good approximation here.

Similarly, the stationary phase approximation applied to the Green's function yields

$$\begin{aligned}G_1(\mathbf{r}, \mathbf{R}') &= \frac{1}{4\pi}B_{rcv}(\mathbf{R}')[1 + \Gamma_{11}(\theta_s)] \\ &\times \frac{\exp(\imath k_1|\mathbf{r} - \mathbf{R}'|)}{|\mathbf{r} - \mathbf{R}'|},\end{aligned}\quad (\text{I.37})$$

where it is convenient here to include the response function for the receiver,  $B_{rcv}(\mathbf{R}')$ , and where  $\theta_s$  is the outgoing grazing angle to the receiver. The grazing angles  $\theta_i$  and  $\theta_s$  are functions of  $\mathbf{R}$ , though that dependence is suppressed.

Next, working from (I.35) one finds

$$\begin{aligned}\left. \frac{\partial \psi_1^{(0)}(\mathbf{r}')}{\partial z'} \right|_{z'=0^+} &= -\imath k_1 p_{src} r_0 B_{src}(\mathbf{R}') \sin \theta_i \\ &\times [1 - \Gamma_{11}(\theta_i)] \frac{\exp(\imath k_1 |\mathbf{R}' - \mathbf{r}_{src}|)}{|\mathbf{R}' - \mathbf{r}_{src}|},\end{aligned}\quad (\text{I.38})$$

where  $\sin \theta_i = z_{src}/|\mathbf{R}' - \mathbf{r}_{src}|$ . Similarly,

$$\begin{aligned}\left. \frac{\partial G_1(\mathbf{r}, \mathbf{r}')}{\partial z'} \right|_{z'=0^+} &= -\frac{\imath k_1}{4\pi} B_{rcv}(\mathbf{R}') \sin \theta_s \\ &\times [1 - \Gamma_{11}(\theta_s)] \frac{\exp(\imath k_1 |\mathbf{r} - \mathbf{R}'|)}{|\mathbf{r} - \mathbf{R}'|}.\end{aligned}\quad (\text{I.39})$$

In these expressions the slow dependence on  $z'$  outside the exponentials was neglected, consistent with the stationary phase approximation.

Finally, working from (I.36) and (I.37) the dot product of horizontal gradients in the third term of (I.34) becomes

$$\begin{aligned} & \nabla'_{\perp} \psi_1^{(0)}(\mathbf{R}') \cdot \nabla'_{\perp} G_1(\mathbf{r}, \mathbf{R}') \\ &= \frac{k_1^2}{4\pi} p_{src} r_0 B_{src}(\mathbf{R}') B_{rev}(\mathbf{R}') \cos \theta_i \cos \theta_s \cos \phi \\ & \quad \times [1 + \Gamma_{11}(\theta_i)][1 + \Gamma_{11}(\theta_s)] \\ & \quad \times \frac{\exp[i k_1(|\mathbf{r} - \mathbf{R}'| + |\mathbf{R}' - \mathbf{r}_{src}|)]}{|\mathbf{r} - \mathbf{R}'||\mathbf{R}' - \mathbf{r}_{src}|}. \end{aligned} \quad (\text{I.40})$$

In obtaining (I.40) the slow dependence on  $\mathbf{R}'$  outside the exponentials was neglected. Also,  $\phi$  is the horizontal bistatic angle between the incident and scattered wave vectors (e.g.,  $\phi = 0$  in the forward direction, and  $\phi = 180^\circ$  for backscatter, or for vertically bistatic backscatter).

Now using (I.36)–(I.40) in (I.34) yields

$$\begin{aligned} \psi_1^{(1)}(\mathbf{r}) &= -\frac{k_1^2 p_{src}}{4\pi} \int_{S_1} dS' A_{rev}(\mathbf{R}') h(\mathbf{R}') \\ & \quad \times \frac{\exp[i k_1(|\mathbf{r} - \mathbf{R}'| + |\mathbf{R}' - \mathbf{r}_{src}|)]}{|\mathbf{r} - \mathbf{R}'||\mathbf{R}' - \mathbf{r}_{src}|}, \end{aligned} \quad (\text{I.41})$$

where  $A_{rev}(\mathbf{R}')$  is given by (2) for bistatic backscattering in the incident vertical plane, i.e., when  $\cos \phi = -1$ . Equation (I.41) gives the final CW result, and it can now be used to obtain a time domain result for the backscattered pressure.

### E. The time domain backscattered pressure

Putting the  $\omega$  dependence explicitly back into (I.41) gives

$$\begin{aligned} \psi_1^{(1)}(\mathbf{r}) &= -\frac{1}{4\pi c_1^2} \int_{S_1} dS' \left[ \frac{A_{rev}(\mathbf{R}') h(\mathbf{R}') p_{src} \omega^2}{|\mathbf{r} - \mathbf{R}'||\mathbf{R}' - \mathbf{r}_{src}|} \right. \\ & \quad \left. \times \exp(i\omega t_{rev}) \right], \end{aligned} \quad (\text{I.42})$$

where  $t_{rev} \equiv (|\mathbf{r} - \mathbf{R}'| + |\mathbf{R}' - \mathbf{r}_{src}|)/c_1$  is the travel time from the source to the point  $\mathbf{R}'$  on the mean plane and then to the field point at  $\mathbf{r}$ . Note that  $A_{rev}(\mathbf{R}')$  has no dependence on  $\omega$  with the assumptions that have been made. It is evident from (2) and (3) that when the frequency dependence of the transducer response functions is neglected, the only possible frequency dependence to  $A_{rev}(\mathbf{R}')$  would enter through  $\kappa = k_2/k_1$ . But when the sound speed in

the sediment is approximated as independent of frequency, and the attenuation in the sediment is approximated as linearly increasing with frequency,  $\kappa$  is independent of frequency.

Finally, inserting (I.42) into (I.4) and performing the inverse Fourier transform leads to (1), where the  $\omega^2$  factor in (I.42) leads to the double time derivative of  $p_{src}(t)$ .

## APPENDIX II TIME DOMAIN IMAGING ALGORITHM

A time-domain image is constructed via a delay and sum beamformer. For a point in the image plane, located at  $\mathbf{r}$ , the coherent, pulse-compressed, baseband pressure is

$$P(\mathbf{r}) = \sum_k A(\mathbf{r}_{sk}, \mathbf{r}_{rk}, \mathbf{r}) \exp(-\imath\omega_0 t_k) P_k(t) \quad (\text{II.1})$$

where  $\mathbf{r}_{sk}$  and  $\mathbf{r}_{rk}$  are the source and receiver coordinates associated with the  $k$ th signal. The corresponding slant ranges to the image point are  $r_{sk} = |\mathbf{r} - \mathbf{r}_{sk}|$  and  $r_{rk} = |\mathbf{r}_{rk} - \mathbf{r}|$ . The amplitude,  $A(\mathbf{r}_{sk}, \mathbf{r}_{rk}, \mathbf{r})$ , contains the beam patterns of the source and receiver as well as compensation for the geometric spreading for the one-way propagation from  $\mathbf{r}_{sk}$  to  $\mathbf{r}$ . Contributions from  $P_k(t)$  that occur outside of the  $-6$  dB down points of the main lobe of the beam patterns are ignored. The exponential factor in (II.1) compensates for spherically diverging waves, and its argument includes the time delay to propagate from the source to an image point and then to the receiver,  $t_k = (r_{sk} + r_{rk})/c_1$ . Finally, co-location of the source and receiver is not required by (II.1), so this beamformer can be used for both monostatic [29] and bistatic SAS [30] applications.

For the SAX04 SAS measurements, the signals are real discrete time signals. In the simulations, only the real part of the complex signal is retained because a generated set of signals is designed to simulate a SAX04 data set. Hence, the complex, pulse-compressed, baseband pressure,  $P_k(t)$ , is obtained by applying a Hilbert transform to  $p_k(t)$ , a matched filter, and removal of the carrier frequency. For SAS processing of the simulated data, the matched filter is constructed from a Hilbert transformed replica of a unit-amplitude transmitted pulse. For the SAX04 data, the matched filter is constructed from a Hilbert transform of the signal applied to the source transducer. The match filter is then normalized to give a pulse-compressed baseband replica with an amplitude of 2.

To form an image, the discrete representation of the image coordinates are

$$x_i = (x_0 - x_l/2) + (i - 1), \quad (i = 1, \dots, N_x), \quad (\text{II.2})$$

$$y_j = (y_0 - y_l/2) + (j - 1), \quad (j = 1, \dots, N_y). \quad (\text{II.3})$$

The center of the image is at  $(x_0, y_0)$ , and the lengths of the sides of the image are  $x_l$  and  $y_l$ . Additionally, the image plane is not confined to the  $z_0 = 0$  plane; however,  $z_0$  is assumed to be constant. For the  $k$ th signal, the slant ranges from the source and receiver to  $(x_i, y_j)$  are

$$r_{skij} = [(x_i - x_{sk})^2 + (y_j - y_{sk})^2 + (z_0 - z_{sk})^2]^{1/2}, \quad (\text{II.4})$$

$$r_{rkij} = [(x_i - x_{rk})^2 + (y_j - y_{rk})^2 + (z_0 - z_{rk})^2]^{1/2}. \quad (\text{II.5})$$

Inspection of (II.1) and the discrete nature of the sampled time signals,  $p_k(t_n)$ , ( $n = 1, \dots, N_t$ ) suggests that  $t_k$  seldom coincides with a discrete time point  $t_n$ . Thus, the summation in (II.1) requires interpolation of the signals. The interpolation has been performed with 2, 4, 6, and 8-point Lagrange interpolation algorithms. Cubic spline interpolation with 6, 12, 24, and 48 points, constructed on intervals centered about a  $t_n$ , were also investigated. Although cubic spline interpolation permitted the construction of an image, 4-point Lagrange interpolation was found to be sufficient for image formation and is more numerically efficient than cubic splines.

#### ACKNOWLEDGMENT

The authors wish to thank all those who developed and operated the APL-UW SAS rail system and STMS2, including R. Light, V. Miller, and M. Kenney. The success of the SAX04 measurement was facilitated by a 24-man APL-UW dive team that provided over 900 hours of diving support in nearly zero visibility conditions. The work reported here depended heavily on the high level of professional expertise shown by the personnel of R/V SEWARD JOHNSON. The authors also enjoyed numerous exchanges with D. Tang and D. Jackson concerning subtle points of the reverberation and penetration models. Finally, this work could not have been accomplished without the funding provided by the Office of Naval Research and the Strategic Environmental Research and Development Program.

#### REFERENCES

[1] J. E. Piper, K. W. Commander, E. I. Thorsos, and K. L. Williams, "Detection of buried targets using a synthetic aperture sonar," *IEEE J. Ocean. Eng.*, vol. 27, pp. 495–504, July 2002.

- [2] J. E. Piper, R. Lim, E. I. Thorsos, and K. L. Williams, "Buried sphere detection using a synthetic aperture sonar," *IEEE J. Ocean. Eng.*, vol. 34, pp. 485–494, 2009.
- [3] See the Special Issue on Sediment Acoustic Processes (Part II), *IEEE J. Ocean. Eng.*, vol. 34(4), pp. 369–515, 2009.
- [4] K. L. Williams, R. D. Light, V. W. Miller, and M. F. Kenney, "Bottom mounted rail system for synthetic aperture sonar (sas) imaging and acoustic scattering strength measurements: Design/operation/preliminary results," in *Proc. of the Inter. Conf. on Underwater Acoustic Measurements: Technologies & Results*, Heraklion, Crete, Greece, June 2005.
- [5] K. L. Williams, S. G. Kargl, E. I. Thorsos, D. S. Burnett, J. L. Lopes, M. Zampolli, and P. L. Marston, "Acoustic scattering from a solid aluminum cylinder in contact with a sand sediment: Measurements, modeling, and interpretation," *J. Acoust. Soc. Amer.*, vol. 127, pp. 3356–3371, 2010.
- [6] E. I. Thorsos, D. R. Jackson, and K. L. Williams, "Modeling of subcritical acoustic penetration into sediments due to interface roughness," *J. Acoust. Soc. Am.*, vol. 107, pp. 263–277, 2000.
- [7] D. R. Jackson, K. L. Williams, E. I. Thorsos, and S. G. Kargl, "High-frequency subcritical acoustic penetration into a sandy sediment," *IEEE J. Ocean. Eng.*, vol. 27, pp. 346–361, Jul. 2002.
- [8] V. C. Anderson, "Sound scattering from a fluid sphere," *J. Acoust. Soc. Am.*, vol. 22, pp. 426–431, 1950.
- [9] G. C. Gaunaud and H. Überall, "Rst analysis of monostatic and bistatic acoustic echoes from an elastic sphere," *J. Acoust. Soc. Am.*, vol. 73, pp. 1–12, 1983.
- [10] G. C. Gaunaud and M. F. Werby, "Lamb and creeping waves around submerged spherical shells resonantly excited by sound scattering," *J. Acoust. Soc. Am.*, vol. 82, pp. 2021–2033, 1987.
- [11] S. G. Kargl and P. L. Marston, "Observations and modeling of the backscattering of short tone bursts from a spherical shell: Lamb wave echoes, glory, and axial reverberations," *J. Acoust. Soc. Am.*, vol. 85, pp. 1014–1028, 1989.
- [12] T. K. Stanton, "Sound scattering by cylinders of finite length. I. Fluid cylinders," *J. Acoust. Soc. Am.*, vol. 83, pp. 55–63, 1988.
- [13] ———, "Sound scattering by cylinders of finite length. II. Elastic cylinders," *J. Acoust. Soc. Am.*, vol. 83, pp. 64–67, 1988.
- [14] L. Flax, G. C. Gaunaud, and H. Überall, "Theory of resonance scattering," in *Physical Acoustics: Principles and Methods*, W. P. Mason and R. N. Thurston, Eds. New York: Academic, 1981, vol. XV, pp. 191–295.
- [15] Z. Ye, "A novel approach to sound scattering by cylinders of finite length," *J. Acoust. Soc. Am.*, vol. 102, pp. 877–884, 1997.
- [16] K. Baik and P. L. Marston, "Kirchhoff approximation for a cylinder breaking through a plane surface and the measured scattering," *IEEE J. Ocean. Eng.*, vol. 33, pp. 386–396, 2008.
- [17] J. J. Bowman, T. B. A. Senior, and P. L. E. Uslenghi, *Electromagnetic and Acoustic Scattering by Simple Shapes*. New York, NY: Hemisphere Publishing, 1987.
- [18] S. G. Kargl and P. L. Marston, "Ray synthesis of the form function for backscattering from an elastic spherical shell: leaky lamb waves and longitudinal resonances," *J. Acoust. Soc. Am.*, vol. 89, pp. 2545–2558, 1991.
- [19] L. G. Zhang, N. H. Sun, and P. L. Marston, "Midfrequency enhancement of the backscattering of tone bursts by thin spherical shells," *J. Acoust. Soc. Am.*, vol. 91, pp. 1862–1874, 1992.
- [20] J. L. Lopes, C. Nesbitt, R. Lim, K. L. Williams, E. I. Thorsos, and D. Tang, "Subcritical detection of targets buried under a rippled interface: Calibrated levels and effects of large roughness," in *Proc. Oceans 2003 MTS/IEEE*, 2003, pp. 485–493.
- [21] ———, "Instrumentation used to conduct controlled measurements of subcritical detection of buried targets," in *Proc. of the Inter. Conf. on Underwater Acoustic Measurements: Technologies & Results*, Heraklion, Crete, Greece, June 2005.
- [22] R. J. Urick, *Principles of Underwater Sound*. New York: McGraw-Hill, 1975.

- [23] L. E. Kinsler, A. R. Frey, A. B. Coppens, and J. V. Sanders, *Fundamentals of Acoustics*, 3rd ed. New York: Wiley, 1882.
- [24] For a given source/receiver pair, the points on the water-sediment interface  $\mathbf{R}$  that can contribute to reverberation satisfy the following criterion:  $(|\mathbf{r}_{rcv} - \mathbf{R}| + |\mathbf{R} - \mathbf{r}_{src}|)/c_1 \leq T$ , where  $T$  is the duration of a recorded signal. The discrete surface realizations generated for simulations were large enough to include all  $\mathbf{R}_{ij}$  for all source/receiver locations along a SAS aperture for which this criterion holds.
- [25] P. T. Gough and D. W. Hawkins, "Unified framework for modern synthetic aperture imaging algorithms," *Int. J. Imag. Sys. Tech.*, vol. 8, pp. 343–358, 1997.
- [26] D. Tang, B. T. Hefner, K. B. Briggs, A. H. Reed, and K. L. Williams, "Measurement of sediment interface and subbottom properties," in *Proceedings of the International Conference - Underwater Acoustic Measurements, Technologies and Results*, Heraklion, Crete, July 2005.
- [27] K. L. Williams, D. R. Jackson, D. Tang, K. B. Briggs, and E. I. Thorsos, "Acoustic backscattering from a sand and a sand/mud environment: Experiments and data/model comparisons," *IEEE J. Ocean. Eng.*, vol. 34, pp. 388–399, 2009.
- [28] D. J. Wingham, "The dispersion of sound in sediments," *J. Acoust. Soc. Am.*, vol. 78, pp. 1757–1760, 1985.
- [29] K. L. Williams, S. G. Kargl, E. I. Thorsos, and D. Tang, "Synthetic aperture sonar (sas) imaging and acoustic scattering strength measurements during sax04 (sediment acoustics experiment – 2004): Experimental results and associated modeling," in *Boundary Influences in High Frequency, Shallow Water Acoustics*, Bath, United Kingdom, September 2005, pp. 139–143.
- [30] S. G. Kargl, K. L. Williams, E. I. Thorsos, and J. L. Lopes, "Bistatic synthetic aperture sonar measurements and preliminary analysis," in *Boundary Influences in High Frequency, Shallow Water Acoustics*, Bath, United Kingdom, September 2005, pp. 127–135.

**Steven G. Kargl** Steven G. Kargl received the B.S. degree in physics and mathematics from the University of Dayton, Dayton, OH, in 1985, and the M.S. and Ph.D. degrees in physics from Washington State University, Pullman, in 1987 and 1990.

For the next three years, he worked as a Research Physicist at the Coastal Systems Station, Naval Surface Warfare Center, Panama City, FL. His research included wave propagation in porous media and ambient noise in littoral waters. In 1993, he joined the Applied Physics Laboratory, University of Washington, Seattle, where he continues to investigate a variety of topics in acoustics. He is currently investigating acoustic penetration into sandy sediments, linear acoustics in a bubbly fluid and nonlinear wave propagation in biological tissue with applications to the formation of thermal lesions. He is currently a Senior Physicist at the Applied Physics Laboratory.

Dr. Kargl is a fellow of the Acoustical Society of America. He served as an Associate Editor for the Journal of the Acoustical Society of America from 2000 to 2003 with Editorial responsibilities in the areas of ultrasonics and physical acoustics.

**Kevin L. Williams** Kevin L. Williams received the B.S., M.S., and Ph.D. degrees in physics from Washington State University, Pullman, in 1979, 1983, and 1985, respectively.

He worked at the Naval Coastal Systems Center, Panama City, FL, from 1985 to 1988, where his primary focus was in acoustic scattering from finite bodies and propagation into ocean sediments. In 1988, he moved to the Applied Physics Laboratory, University of Washington, Seattle, where he has worked in the area of high-frequency environmental acoustics, studying propagation through ocean internal waves and arctic ice and propagation and scattering in ocean sediments. He is currently a Principal Physicist the Applied Physics Laboratory. He is also an Associate Professor in the Oceanography Department, University of Washington.

Dr. Williams is a Fellow of the Acoustical Society of America.

**Eric I. Thorsos** Eric I. Thorsos received the B.S. degree in physics from Harvey Mudd College, Claremont, CA, in 1965, the M.S. degree in engineering and applied science from the University of California, Davis-Livermore, in 1966, and the Ph.D. degree in theoretical nuclear physics from the Massachusetts Institute of Technology, Cambridge, MA, in 1972.

From 1972 to 1975, he was an Assistant Professor of physics at Hobart and William Smith Colleges, Geneva, NY; from 1975 to 1980, he worked in the area of inertial confinement fusion at the Laboratory for Laser Energetics at the University of Rochester, Rochester, NY; and since 1980, he has worked in underwater acoustics at the Applied Physics Laboratory, University of Washington, Seattle. He is presently a Principal Physicist at the Applied Physics Laboratory and Associate Research Professor in the Electrical Engineering Department, University of Washington. His research interests include acoustic scattering from the sea surface and the sea bottom, and he was Chief Scientist on SAX99 and SAX04.

Dr. Thorsos is a Fellow of the Acoustical Society of America, and received the Bronze Medal from the National Defense Industrial Association in 1999.